The International Journal of Advanced Manufacturing Technology (2023) 125:25–46
https://doi.org/10.1007/s00170-022-10758-3

CRITICAL REVIEW

Research and prospect of on-line monitoring technology for laser additive manufacturing

Wanyang Li[1] · Weiwei Liu[1] · Kazi Mojtaba Saleheen[1] · Huanqiang Liu[1] · Yong Xia[1,2] · Gamal Al-Hammadi[1] · Lin Xue[1] · Fengtao Wang[3] · Xueguan Song[1] · Yingzhong Zhang[1]

Received: 3 September 2022 / Accepted: 19 December 2022 / Published online: 29 December 2022

Abstract
This paper mainly discusses the current research status and development trend of on-line monitoring technology for laser additive manufacturing. We have analyzed various on-line monitoring techniques for laser additive manufacturing based on visual imaging, temperature field, spectral analysis, and acoustic principles. Numerous analyses are performed on the monitored objects, the melt pool, including melt pool temperature and morphology dimensions, and the formed parts, including microstructure and properties. The analysis of on-line monitoring techniques for laser additive manufacturing is expected to find the research directions that meet future development trends.

Keyword Laser additive manufacturing; on-line monitoring; on-line monitoring techniques; Monitored objects; Future development trends

1 LAM on-line monitoring technology

Based on the 3D model data of the part and the laser processing heat source, laser additive manufacturing (LAM) is an emerging material processing technology that directly create solid parts through layer-by-layer stacking of materials. This technology has been widely used in various fields due to the wide range of materials, short manufacturing cycles, low environmental pollution, and easy manufacturing of parts with complex structures [1–3]. The main processing methods of LAM include laser cladding deposition (LCD), selective laser melting (SLM), and selective laser sintering (SLS) [4, 5]. LAM can form functionally graded parts with specific organizational components in different parts by a variety of materials, so as to achieve the purpose of regulating the performance. Non-equilibrium physical metallurgy and thermophysics are very complex AM processes, which are accompanied by the interaction of laser, powder, matrix, and melt pool. The rapid solidification and shrinkage of the melt pool produce large temperature gradients. And the periodic, violent, and non-stationary cyclic heating, cooling, and short-time non-equilibrium cyclic solid-state phase transformation of the high-energy laser beam produce residual thermal stresses and stress concentration in part, resulting in warping deformation and cracking, and the internal defects such as micro-cracks and micro-pores, which seriously affect the microstructure and the mechanical properties [6–9]. Therefore, on-line monitoring of LAM can repair the defects that may occur in AM by regulating various parameters, which greatly improves the quality. On-line monitoring technology can realize real-time recording of the whole process and multi-directional of LAM. Firstly, through on-line monitoring, the location and type of defects can be quickly found and then judge whether it seriously affects the production of the parts. Secondly, we can repair the defects on-line by modifying the process path and various process parameters [10] to improve the qualified rate. Finally, through on-line monitoring process data, it can study the LAM process mechanism and optimize the process parameters, laying the theoretical foundation for the next practical production.

✉ Weiwei Liu
ghostliuww@163.com

[1] School of Mechanical Engineering, Dalian University of Technology, Dalian 116024, China

[2] Power Machinery and Electricity (Dalian) Co., Ltd, Dalian 116602, China

[3] Department of Mechanical Engineering, College of Engineering, Shantou University, Shantou 515063, China

1.1 Visual imaging-based on-line monitoring

The visual imaging-based on-line monitoring technology almost always adopts the structured light method, which mainly monitors the various size parameters of the melt pool morphology on-line, and establishes a feedback control system to reduce macroscopic defects such as size abnormality and deformation. LAM is essentially the laser melting and solidification of materials, which is similar to the welding process. Therefore, the visual imaging-based on-line monitoring technology for LAM follows the methods and principles of welding on-line monitoring. CCD is superior to CMOS in sensitivity, resolution, and noise control, while CMOS has the characteristics of low cost, low power consumption, and high integration. CCD should have high sensitivity and higher resolution. CMOS have more complex pixels, but there is a lot of noise, which affects the image quality.

Based on the principle of the industrial camera (CCD), passive visual imaging, and the structural light active visual imaging, Heralic et al. [11] developed a LAM on-line monitoring system to obtain the height information of the coating. Using the on-line monitoring closed-loop feedback control system developed by an industrial camera (CMOS), Hofman et al. [12] regulated the laser power through the width information of the coating and then realized the control of the formed dimensions. The melt pool image was acquired, and the position was determined by a CMOS camera shooting at 45° to the melt pool based on the empirical threshold method. After image processing and filtering, the melt pool width information was obtained. The laser power was controlled to obtain the ideal pool dimension, the small dilution rate, and the uniform pool width. Using the on-line monitoring closed-loop feedback control system developed by an industrial camera (CCD) and a dual-color high temperature multi-signal controller, Li et al. [13] achieved the on-line control of the coating height. The closed-loop feedback control system of on-line monitoring of the melt pool by an industrial camera (CCD) can obtain the width information, and then Arias et al. [14] regulated the laser power. Kanko et al. [15] monitored the melt pool morphology dimensions of SLM on-line by low-coherent interferometry imaging technology and reduced the deformation by on-line monitoring closed-loop feedback control system. Tang et al. [16] established an on-line monitoring closed-loop feedback control system of the coating height and powder feeding rate, in which the monitoring data, melt pool temperature, and powder feeding rate was taken as control variables to achieve stable forming of the height.

Based on the industrial camera (CMOS), Barua et al. [17] proposed a method to monitor internal defects on-line by photographing and observing the red hot melt channel, inferring that the existence of the internal defects was related to the brightness. However, the visual imaging-based on-line monitoring technology for LAM has less research on internal defect monitoring, which will become a research hotspot in the future.

1.2 Temperature field-based on-line monitoring

LAM on-line monitoring technology is not only based on the visual imaging, but also based on the temperature field through the acquisition and analysis of melt pool temperature data. The on-line monitoring technology consists of the single temperature data and the melt pool temperature by an infrared camera to provide feedback on the melt pool morphology and dimension. At present, the main monitoring methods of the melt pool temperature in LAM mainly include contact thermometry and non-contact thermometry. Contact thermometry has the advantages of low cost and accurate measurement, but it has the disadvantages of not being able to measure the melt pool and slow response directly. It is often used to validate the melt pool values for simulation experiments and to help in the setting of boundary conditions. Thermo-couple thermometry is the main method of the contact temperature measurement. Non-contact thermometry is based on the radiation measurement, in which sensor cost is high. Monochromatic pyrometer thermometry, colorimetric pyrometry thermometry, and CCD-infrared image thermometry are the main methods of the non-contact thermometry [18]. Fuzzy logic control, generalized predictive control, PID control, and its improved control algorithms have played an important role in controlling the melt pool temperature while improving the processing quality of the parts to a great extent. The stability of the melt pool temperature is an extremely critical indicator to characterize the stability. The effective and stable control of melt pool temperature plays a decisive role in improving the geometric accuracy and macroscopic mechanical properties, and optimizing the microstructure. Therefore, it is of great significance to establish a closed-loop feedback control system, monitor the melt pool temperature on-line, adjust the process parameters, and control the stability of the melt pool temperature.

Hu et al. [19] measured the temperature at different positions of the melt pool by thermo-couple thermometry. Lin et al. [20] measured the surface temperature of the melt pool with an infrared thermometer for the boundary temperature. In order to calculate the surface temperature of the melt pool, Li et al. [21] installed photodiodes on the side of the melt pool to receive the light signal. Song et al. [22] used the two-color pyrometer to detect and feedback control the melt pool temperature. In order to accurately measure the melt pool temperature, Pavlov et al. [23] combined a

multi-wavelength thermometer with an infrared camera to measure the temperature at a certain angle to the melt pool. Hu et al. [24] photographed the melt pool with an infrared camera coaxially mounted on the cladding equipment for the accurate area. Hu et al. [25] designed a closed-loop feedback control system that can control the heat input and melt pool dimension with the infrared thermal imager. The on-line monitoring based on temperature field has the advantages of simple operation and easy temperature measurement in the molten pool area, but the effective information obtained is less, which cannot be used as the main basis. However, the inspection of the melt pool by the infrared thermal imager can only measure the geometry and appearance, which cannot reflect the internal defects. Moreover, infrared imaging devices limit the research and application of temperature field-based on-line monitoring because of the high cost and the requirement that the emissivity parameters must be maintained with high accuracy.

1.3 Spectral analysis-based on-line monitoring

In the LAM process, the generation of part defects is highly dependent on the material composition and element content, so the spectral analysis-based on-line monitoring technology has been developed to monitor the material composition and elements, which can effectively identify defects. In the process of laser additive manufacturing, spectral analysis-based on-line monitoring is to analyze the characteristic spectral line intensity, characteristic spectral line intensity ratio, plasma temperature, and electron density of the photoinduced plasma collected by the spectrometer to reflect the internal conditions of the plasma.

Scharun et al. [26] developed a portable LIBS analyzer based on a pulsed laser, which can quantitatively analyze ferroalloy. The spectral characteristics of Al under different laser wavelengths were studied by LIBS. Abdellatif et al. [27] found that the plasma parameters, electron temperature, and electron density can be changed by controlling the laser wavelength, which significantly improved the feasibility of LIBS element detection. Barnett et al. [28] investigated the spectral characteristics change and ablation under laser excitation at 266 nm and 532 nm. The results showed that the sample had more ablation amount and higher calibration accuracy under laser excitation at 266 nm, while stronger spectral lines could be excited at 532 nm. Fornarini et al. [29] combined theories and experiments in alloy samples, which studied the effects on the properties under laser excitation at 1064 nm and 355 nm. When the laser wavelength was 1064 nm, the sample surface temperature decreased due to the strong plasma absorption. When the energy reaching the sample surface was low, the shielding effect of the plasma occurred. Therefore, a more intense spectrum was obtained at 1064 nm. Lu et al. [30] investigated the variation of the melt pool composition by spectral monitoring. When Inconel 625 metal powder was deposited, the spectral information was collected by changing the process parameters (laser power and scanning speed), respectively. It was found that all of them were able to obtain strong characteristic spectral lines of Cr, which meant that the melt pool contained a large amount of Cr. This study provided a good basis for predicting the complex element composition and content in the melt pool. Shin et al. [31] monitored the composition changes during laser metal deposition by spectroscopic diagnostic techniques. When the Inconel 718 metal powder and pure Cr powder were deposited, the relative content of Ni was changed by varying the content of pure Cr powder. The relationship between the plasma temperature and the intensity ratio of the four characteristic spectral lines and the content of Ni was established by analyzing the spectral information, as shown in Fig. 1. The plasma temperature was found to decrease with the increase of Ni, and the intensity ratios of all four characteristic spectral lines increased with the increase of Ni. It was found that the prediction accuracy of the characteristic spectral line intensity ratio for Ni content was higher than that of the plasma temperature, which could accurately predict the composition. Therefore, in order to improve the accuracy and sensitivity of spectral analysis-based on-line monitoring, reasonable monitoring process parameters as well as suitable monitoring data processing methods need to be selected in component monitoring.

1.4 Acoustic-based on-line monitoring

In the process of LAM, each defect generated can emit acoustic signals with unique characteristics. Using appropriate sensors to collect and identify the defect types corresponding to different signals is a key problem for the

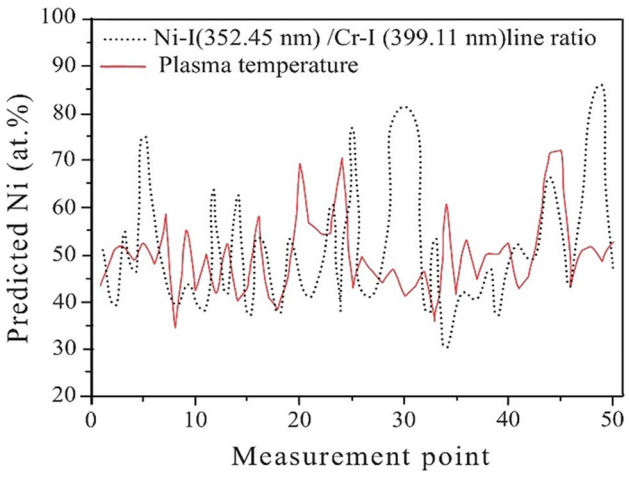

Fig. 1 Ni-I352.45 nm/Cr-I399.11 nm characteristic line intensity ratio prediction curve [31]

defect on-line monitoring, and it is also an important link in controlling part quality. The propagation of the vibration generated by the sound generator in the air or other materials is called sound waves. Sound waves travel in all directions through various media, which are usually longitudinal waves and also shear waves. The types of sound waves include plane acoustic waves, spherical acoustic waves, and cylindrical acoustic waves.

Plotnikov et al. [32] monitored the LAM process by the acoustic sensors and the infrared thermal imager, established the relationship between the image and the acoustic signals, and studied the relationship between the acoustic signal characteristics and the porosity, as shown in Fig. 2. Lee et al. [33] used fiber Bragg grating sensors to collect acoustic signals in LAM process, established the relationship between the acoustic signals and the porosity, and realized the porosity monitoring that based on the acoustic signals. Gaja et al. [34] monitored the crack defects in LAM by acoustic signals and found that the crack-induced acoustic signals had short time intervals and large amplitudes. Kouprianoff et al. [35] used the 378B02 microphone to monitor the powder laying height. Shevchik et al. [36] analyzed the data based on a wavelet, identified the defects based on deep learning, and predicted the quality of each layer based on acoustic signals. However, in the process of metal deposition, droplet transfer, melt pool flow, and shielding gas flow will produce sound, which is complex and difficult to separate. The acoustic signal has a low resistance to environmental interference which is vulnerable to environmental noise. Therefore, it is difficult to quantitatively establish the relationship between the acoustic signal, the forming quality, and the forming stability. Ultrasonic imaging technology has been used for on-line monitoring, which can monitor internal defects along with quantitative detection, but the equipment cost was high. Cerniglia et al. [37] successfully detected micro-defects with a diameter of 0.1 mm and large defects with a depth of less than 0.8 mm on the single deposition layer sample surface by the laser ultrasonic testing and verified the detection results by the high-sensitivity X-ray technology. In summary, acoustic-based on-line monitoring of LAM can monitor defects. At the same time, the extraction of signal characteristics can further establish the corresponding relationship between the signal characteristics and the defects.

2 On-line monitoring of the melt pool

2.1 Melt pool temperature

The variation of the melt pool temperature leads to the instability of the melt pool morphology and dimension, and the melt pool temperature also affects the geometric accuracy of the deposition layer. The flow of the melt pool leads to the reduction of forming accuracy, the change of porosity and dilution rate, and the deterioration of surface forming quality. The unstable melt pool temperature will affect the distribution of the temperature field, resulting in the generation of thermal residual stress, the deformation of overall stress,

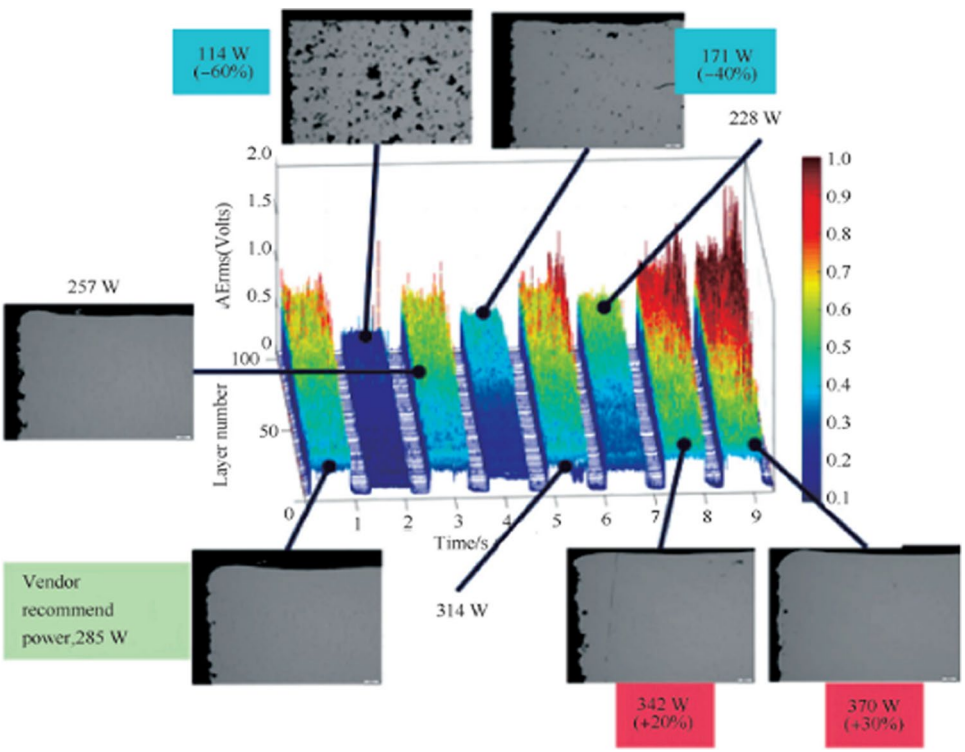

Fig. 2 Corresponding acoustical signal with different porosity during SLM [32]

the change of solidification structure, and the deterioration of mechanical properties. The porosity and the dilution rate between the matrix and the forming part are directly affected by the melt pool temperature. If the melt pool temperature is too low, the powder will not be fully melted, which will easily produce defects such as porosity, and if the temperature is too high, which will cause the too large dilution rate. The heat-affected zone (HAZ) and dilution ratio will be increased with the increase of melt pool temperature, resulting in thermal deformation and thermal residual thermal stress cracking. The occurrence of cracks, over-melt, and under-melt can be effectively reduced by controlling the melt pool temperature. The melt pool temperature also has an important influence on the microstructure. By controlling the melt pool temperature, the generation of hard and brittle phases can be effectively reduced, so as to improve the mechanical properties.

Many scholars have predicted the crystal growth direction [38, 39], thermal residual stress, thermal residual deformation [40, 41], and temperature gradient [42] by simulating the temperature field. Therefore, the on-line monitoring of the melt pool temperature can not only ensure the forming accuracy and quality, but also play an important role in improving the melt pool morphology and dimension as well as the mechanical properties. Based on the two-color infrared pyrometer, Tan et al. [43] established an on-line melt pool temperature measurement system to achieve on-line monitoring. At the same time, it lays a foundation for the following on-line feedback control of the melt pool dimension. Bi et al. [44] established a path-based variable energy input closed-loop feedback control system of laser power by Ge photodiode which improved the thickness and the accuracy of thin-walled parts. Tang et al. [45] established a closed-loop feedback control system of laser power based on the melt pool temperature signal by the temperature sensor, which used the temperature signal as the feedback to adjust the laser power. During the part forming process, Salehi et al. [46] established the on-line monitoring and closed-loop feedback control system of melt pool temperature by PID on-line feedback, which effectively maintained the stability and improved the accuracy and quality.

Devesse et al. [47] used the hyperspectral camera to monitor the melt pool temperature on-line and the measurement setup as shown in Fig. 3. The laser power was adjusted in real time according to the feedback information, and the melt pool temperature and dimension were kept highly stable by the on-line feedback and the PI control. The performance of the control system was evaluated by heating the matrix from room temperature to 1 mm width. The experimental results are shown in Fig. 4. First, it can be seen that the estimated melt pool boundary is very consistent with the simulated melt pool boundary, which verifies the stability of the closed-loop feedback

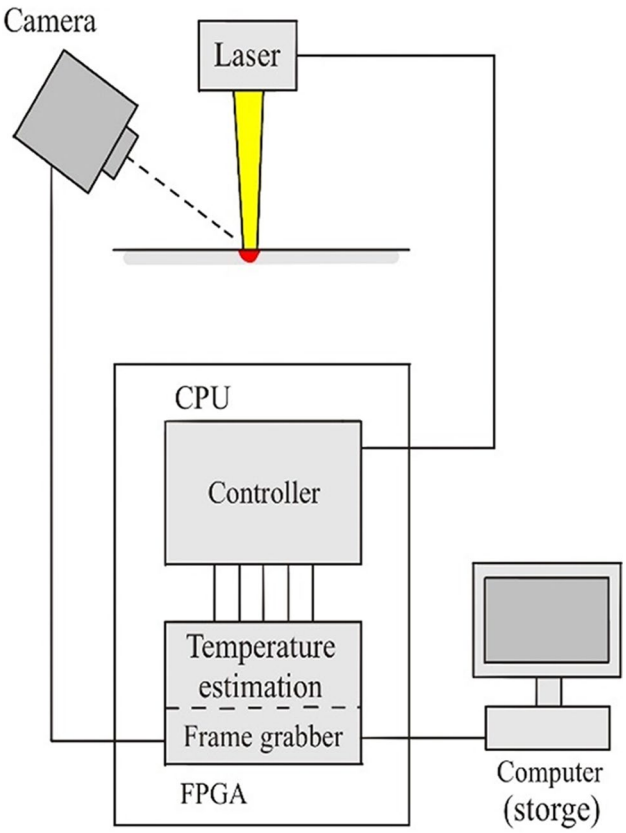

Fig. 3 Measurement setup [47]

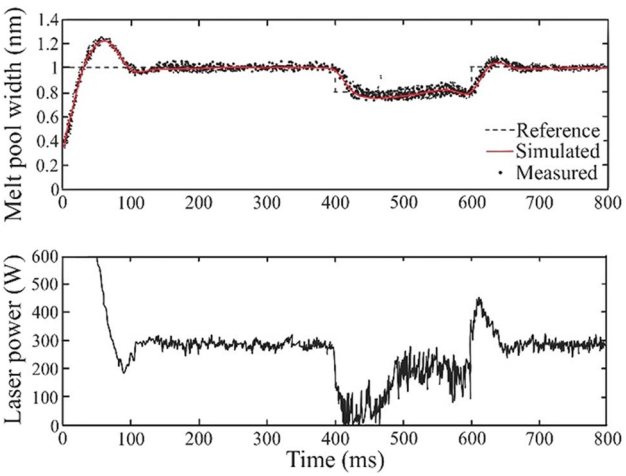

Fig. 4 Hardware-in-the-loop results showing the accuracy of the estimated melt pool width and the performance of the controller with a varying reference [47]

control system. The control system can accurately determine the position of the melt pool boundary through the image generated by constant emissivity and the careful calibration by the computer monitor and camera. If either

of the two conditions is not completely satisfied, the estimated temperature may deviate from its true value.

Song et al. [48] designed a series structure of a melt height controller and a melt temperature controller that can realize dual-signal input and single-signal output laser power to precisely control the coating height by using the three high-speed CCD cameras that 120° distributed and the two-color pyrometer that measured the melt pool height and temperature, respectively. The hybrid controller based on the two-color pyrometer and the high-speed camera that made the melt pool height increase steadily and reduced the melt pool height error between the each layer and the specified layer. Figure 5a shows the turbine blades that with and without control, and the width of the turbine blade gradually decreases from the middle to the tail. Under the constant laser power, the narrower part near the end accumulated more heat than the wider part near the front. As the number of the deposited layers increased, the volume gradually increased, and the heat dissipation rate gradually became slower, which increased the heat accumulation. The melt pool temperature near the end was higher, which reduced the deposition height and generated the larger melt pool. In the absence of temperature control, the top surface bent upward because the powder collection efficiency at the flat was higher than the edge. Excessive heat accumulation and high powder collection efficiency resulted in the severe deformation and even prevented further deposition. Defects caused by uneven heat accumulation and unstable powder collection efficiency can be avoided by the laser deposition that with stable heat input and controlled melt pool height. The melt pool temperature is stabilized at around 1700 °C by the temperature controller, and the laser power is dynamically changed to avoid excessive heat accumulation in the narrow areas (Fig. 5b). In the experiment, the parts with small edge curvature were obtained by temperature control, and in the closed-loop feedback controlled process, the turbine blade formed by hybrid controller that had a better near net shape and dimensional accuracy.

Through the temperature controller, the experiment set the constant temperature reference value and the time-dependent temperature and kept the powder feeding rate constant [49]. In the experiment of tracking the constant temperature reference, the average absolute error was reduced by 52.3%, and the temperature controller worked well, which greatly reduced the temperature error. As can be seen in Figs. 6 and 7, the temperature controller suppresses the rising trend of the melt pool temperature that rise along the deposition track.

In the experiment of tracking the time-dependent temperature reference, there was no significant change in the mean absolute error and the standard deviation of the error compared to the constant temperature reference. Compared with the open-loop control, the average absolute error and the standard deviation of the error were reduced by 65.5% and 58.1%, respectively. The results show that the temperature controller worked well when tracking the time-dependent

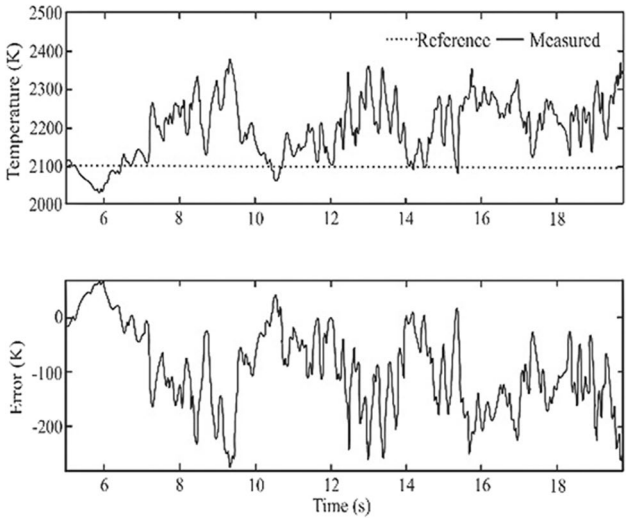

Fig. 6 Open-loop temperature response for $T_r(t) = 2100$ K with $q = 537.6$ W, $m = 6$ g/min, and $v = 2.54$ mm/s[49]

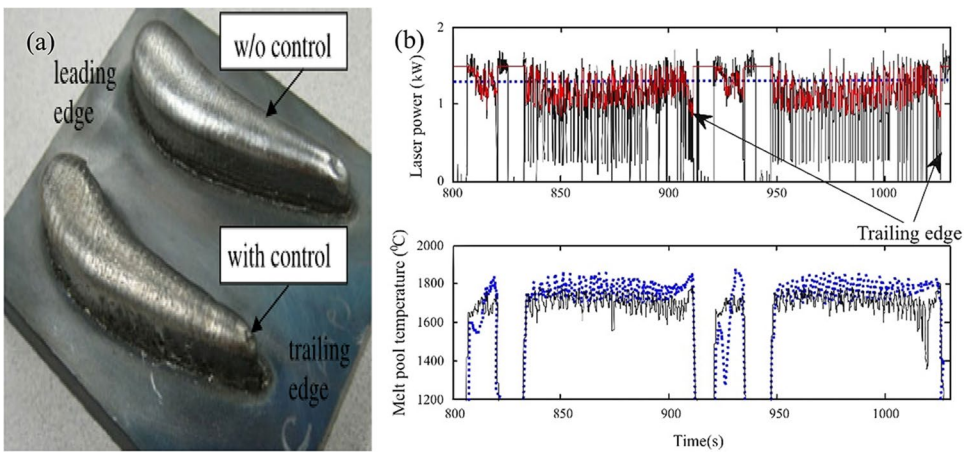

Fig. 5 **a** Turbine blades that with and without control; **b** melt pool temperature during the eighth and ninth contour and layer deposition. Upper figure, dotted without control; solid gray height control, solid red temperature control. Lower figure, dotted without control, solid with control [48]

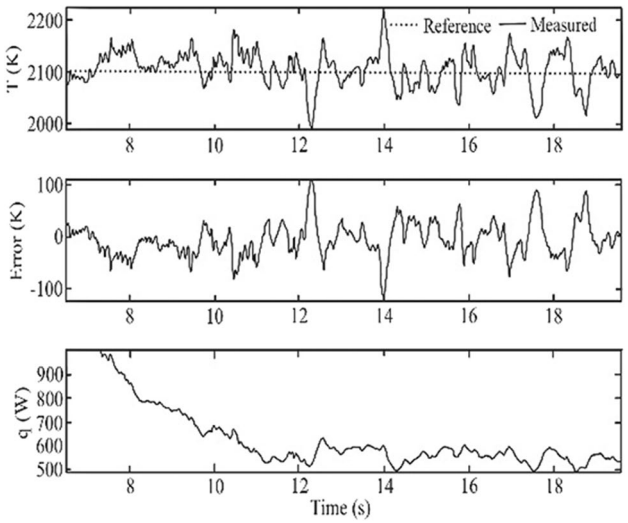

Fig. 7 Closed-loop temperature response for $T_r(t) = 2100$ K with $m = 6$ g/min and $v = 2.54$ mm/s [49]

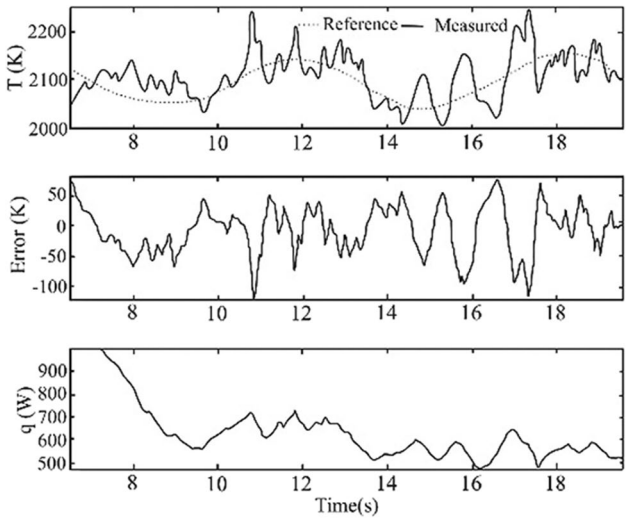

Fig. 9 Closed-loop temperature response for $T_r(t) = 2100$ K + 50sin(t) K with $m = 6$ g/min and $v = 2.54$ mm/s [49]

temperature reference, and the temperature error was greatly reduced. By comparing the open-loop and closed-loop temperature control, it can be seen that the constant process parameters cannot accurately adjust the melt pool temperature (Figs. 8 and 9).

2.2 Melt pool morphology and dimension

The ideal cross-section morphology of the single-layer melt pool with good metallurgical bonding, small dilution rate, and large aspect ratio is conducive to stabilize the multi-track overlapping and multi-layer stacking, which reduced the forming time and the porosity and improved

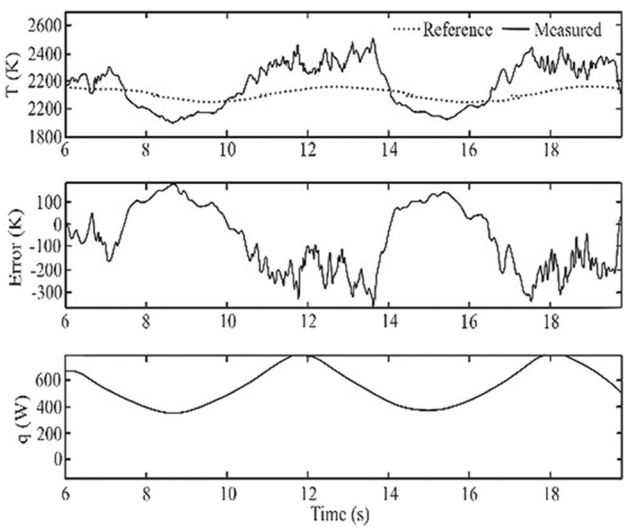

Fig. 8 Open-loop temperature response for $T_r(t) = 2100$ K + 50sin(t) K with $m = 6$ g/min and $v = 2.54$ mm/s [49]

the forming efficiency and the forming quality. There are two main closed-loop feedback control methods for on-line monitoring of melt pool morphology and dimension. The first method is to adjust the process parameters timely according to the comparison results that after comparing the ideal value with the on-line melt pool information, so as to stabilize the melt pool dimension. Through an image processing algorithm, Asselin et al. [50] used the CCD camera to photograph the melt pool in a distributed manner, which achieved on-line monitoring of the melt pool dimension. Song et al. [51] used the CCD camera to shoot the melt pool in the same way, which extracted the boundary and obtained the dimension. Through a large number of experiments, the closed-loop feedback control has the advantages of higher melt pool stability, rapid response time, and high forming accuracy. However, the accuracy error generated by layer-by-layer accumulation is large, so it is unable to ensure the final accuracy. The second method is to make the result converge to the ideal value by adjusting the accumulated error. By means of the variable structure controller, Fathi et al. [52] achieved the closed-loop control of the melt pool morphology. Through the combination of the CCD camera and the image processing, Zeinali et al. [53] obtained the coating height feedback signal that controlled the speed of the workbench. Through the CCD lens with 1064-nm band-stop filter and 700-nm long-pass filter, Moralejo et al. [54] acquired the melt pool images. At the same time, the laser power was selected as the output of the feedforward PI, which accelerated the control response and obtained the ideal dimension. Although the closed-loop feedback control method has a slow response, it increases the feedforward control path and considers the delay time, which improves the response

Table 1 Experimental parameters in numerical simulation [55]

Experimental parameters	Value
Laser power (W)	900–1900
Spot size (mm)	5
Cladding speed (mm/s)	4
Cladding length (mm)	70
Uplift (mm/layer)	0.5
Powder feeding rate (g/min)	7.41

Fig. 10 Results of single-channel liner cladding experiment under different powers [55]

to some extent and reduces the overshoot. Further, the control method can ensure the high forming accuracy.

By designing single-channel liner cladding experiments under different powers, melt pool morphology, and dimension variation were observed [55]. The experimental parameters are shown in Table 1, the experimental results are shown in Fig. 10, and as layers increase, the variation of the melt pool width and length under different powers are shown in Fig. 11a and b, respectively. As the power and layers increase, the melt pool width and length gradually increase. When the power is 900 W, the melt pool width starts to be larger than the spot diameter after the 8th layer. When the power is 1100 W, the melt pool width starts to be larger than the spot diameter after the 4th layer. When the power is 1300 W, the melt pool width starts to be larger than the spot diameter after the 2nd layer.

When the power is 1500 W, the change of the melt pool width and length at different points in the 8th layer is shown in Figs. 12a and b, where the spot diameter is 5 mm. When the scanning direction changes at the end of the workpiece, the width reaches the maximum, and the length reaches the minimum because of the short-term reciprocating scanning in the same region. The melt pool length becomes shorter at the end of the workpiece because the direction of the laser head has the greater effect, and the melt pool width has the accuracy in reflecting the information. The experiments show that the melt pool width is more suitable for extracting the information. When the direction changes, the melt pool length will be instantaneously shortened, and the power will be increased according to the PID, which aggravates the excessive melting at the end of the workpiece.

By analyzing the variation of the melt pool under the different parameters, Ocylok et al. [56] found that the most significant factor that affected the melt pool was the laser power, and the single-pass deposition method was proposed based on the laser power adaptive control. Tabernero et al. [57] reduced the average error between the predicted and the measured of the melt pool height and width by calculating the hydrodynamic model and the heat source-based laser deposition model. Through establishing the closed-loop feedback control system that based on the PID controller and the feedback compensation, Ding et al. [58] made the dimension uniform.

The model between the laser power, the scanning speed, the powder feeding rate, and the melt pool dimension was established in the experiment [59]. The results of the parameters and the melt pool width are shown in Table 2. It is found that the maximum error rate is less than 4.5%, and

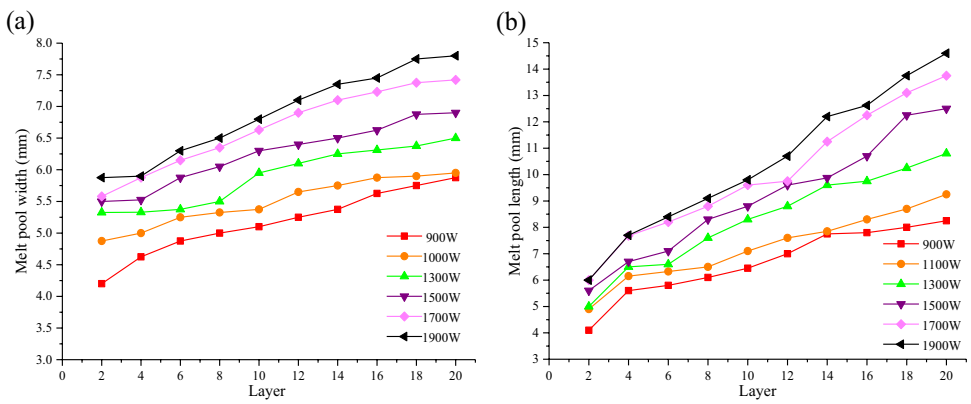

Fig. 11 As layers increase, the variation of melt pool width and length under different laser powers **a** melt pool width; **b** melt pool length [55]

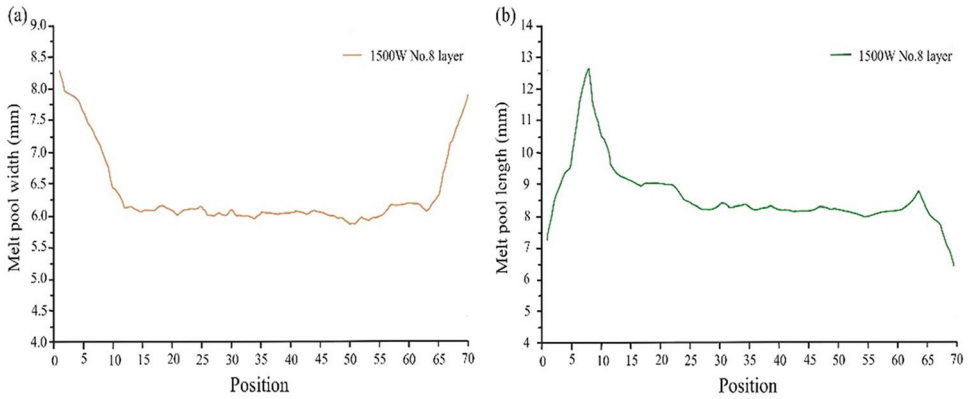

Fig. 12 Variation of melt pool width and length at different positions of layer 8 of 1500 W **a** melt pool width; **b** melt pool length [55]

Table 2 Process parameters and experimental results of each deposition channel [59]

No	P (W)	v (mm·s^{-1})	Q_m (g·min^{-1})	Melt pool width (mm)		
				Measured	**Calculated**	**Error (%)**
1	2000	7	7.2	4.65	4.44	4.5
2	2200	15	3.3	4.13	4.00	3.1
3	2200	9	7.2	3.97	4.16	4.2
4	2200	13	11.1	4.19	4.13	1.4
5	2200	11	9.1	4.17	4.28	2.3
6	2000	9	9.1	4.18	4.21	0.9
7	1800	13	5.2	3.71	3.65	1.6
8	1400	9	5.2	3.29	3.38	2.7
9	2000	15	5.2	3.68	3.77	2.4
10	1800	11	3.2	3.82	3.78	1.0
11	2200	7	5.2	4.77	4.70	1.5
12	1600	15	9.1	3.16	3.28	3.7
13	1800	15	7.2	3.49	3.53	1.1
14	1800	9	11.1	3.79	3.95	4.2
15	1600	13	7.2	3.30	3.38	2.7
16	2000	13	3.3	4.01	3.89	2.9
17	1600	9	5.2	3.63	3.51	2.3
18	1400	7	3.3	3.60	3.57	0.8
19	1600	7	11.1	3.83	3.88	1.3
20	1400	13	9.1	3.20	3.11	2.8
21	1600	9	3.3	3.80	3.67	3.4
22	1800	7	9.1	4.42	4.37	1.1
23	2000	11	11.1	4.11	4.04	1.9
24	1400	11	7.2	3.11	3.23	3.8
25	1400	15	11.1	3.16	3.05	3.4

the width under different parameters can be accurately predicted. With the increase of laser power, the width gradually increases, and with the increase of scanning speed, the width gradually decreases. In the above parameters, the laser power has the significant effect.

In order to verify the correctness of the above analysis, and investigate the effect of each parameter on the width. The single variable method was used to increase the parameters, the parameters and each level values are shown in Table 3.

Table 3 Process parameters and each level values [59]

Parameters	Levels of parameters			Other parameters	
	1	**2**	**3**		
P (W)	800	1600	2400	$v=10$	$Q_m=6$
V (mm·s^{-1})	5	10	15	$P=1600$	$Q_m=6$
Q_m (g·min^{-1})	3	6	19	$P=1600$	$v=10$

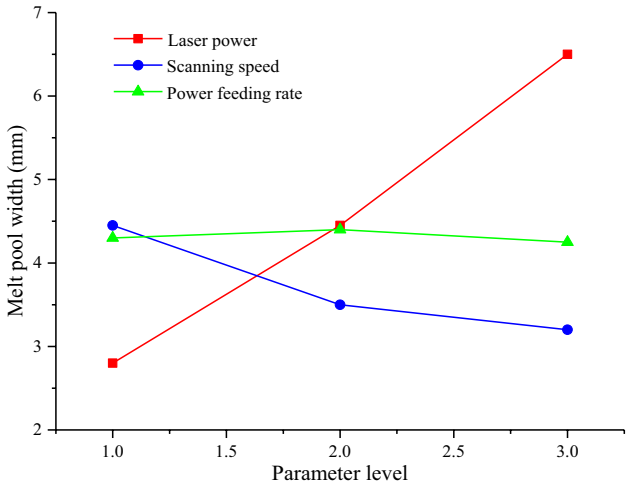

Fig. 13 Melt pool width for different process parameter levels [59]

Figure 13 shows the effect of each parameter on the melt pool width. It can be seen from the figure that among the various process parameters, the power has the most influence, the scanning speed has the less fluctuation, and the powder feeding rate has almost no effect. Meanwhile, the experimental results of the positive correlation between the laser power and the width as well as the negative correlation between the width and the scanning speed verify the correctness. In order to avoid melt pool variations caused by local geometry, optical sensors were used to continuously monitor the melt pool in the LAM process [60, 61]. These sensors will provide feedback on the dimension information to the real-time circuit, and the required dimension characteristics will be obtained by adjusting the parameters. Optical sensors were used to monitor the dimension on-line, and the laser power was controlled by feedback, which reduced the fluctuation in the melt pool temperature and improved the surface quality. Craeghs et al. [62] designed an on-line monitoring closed-loop feedback control system to monitor the melt pool morphology on-line by the optical sensors, and the laser power was adjusted on-line by feedback data, which improved the appearance. Figure 14 shows the melt pool area, length and width, and the photodiode signal. It can be seen that the photodiode signal and the area show a good correlation. The photodiode signal peak is more flattened compared with the calculated characteristics.

The information on the thermal radiation intensity from the melt pool was collected on-line; Miyagi et al. [63] established an on-line closed-loop feedback control system of thermal radiation intensity and laser power by adaptive PID, which improved the dimensional accuracy. Using three diodes integrated into the laser head, the signal of thermal radiation, smoke radiation, and laser energy reflected by melt pool were monitored on-line. The photodiode was used to monitor the thermal radiation on-line, and an adaptive feedback control system of laser power was established according to the thermal radiation intensity, which improved the dimensional accuracy of the 316L stainless steel specimen. The experimental equipment is shown in Fig. 15.

Fig. 14 Typical output of the process sensors: melt pool area, length and width, and the photodiode signal [62]

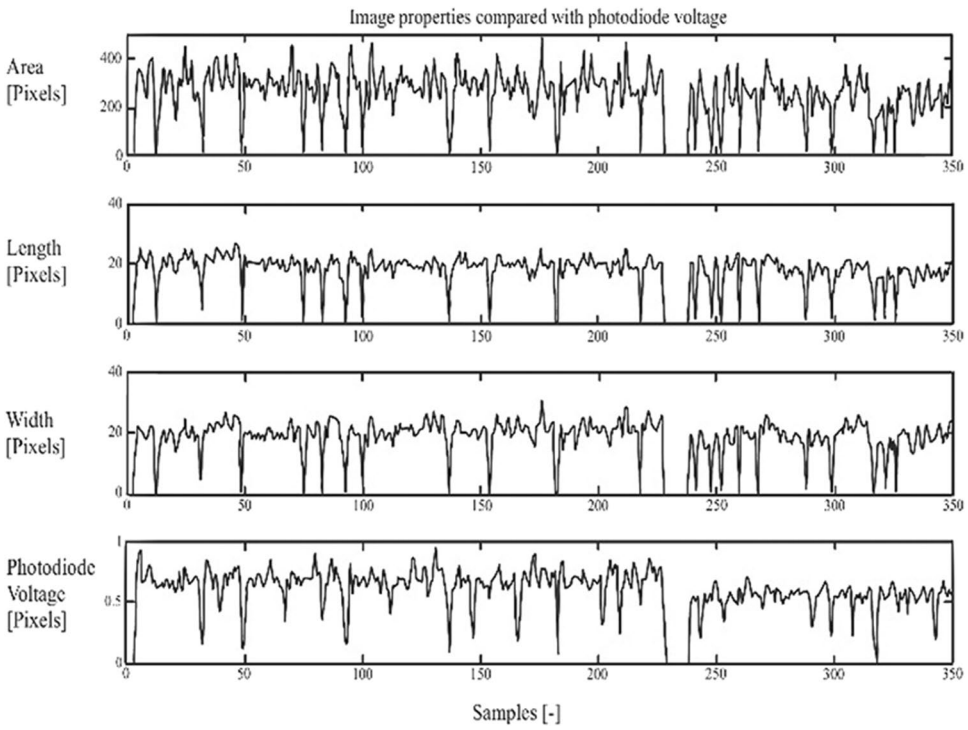

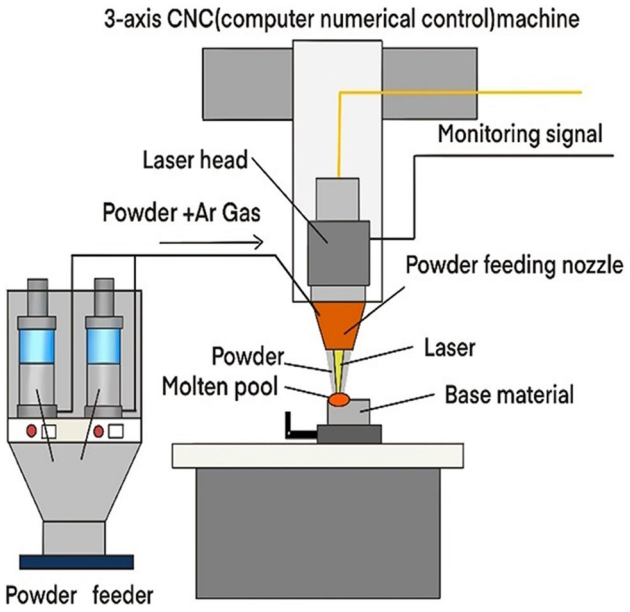

Fig. 15 Experimental setup for LMD process [63]

The relationship between the dimension structure characteristics and the single deposition layer monitoring information was studied. Figure 16 shows the cross-section of the melt pool under different powers (1000–1700 W) and the observation of the CCD camera. The observation shows that the melting area increases gradually with the power increases. It proves that the results are well correlated with the cross-section, and the dimension varies with the power. During the single-deposition layer testing, the average signal strength was used to characterize the relationship between the signal strength and the laser power based on the each monitored intensity stability characteristics. The thermal radiation signal intensity was used to represent the temperature relative change in the melt pool area. Figure 17a shows the relationship between the signal intensity and the laser power. It can be seen that the average signal intensity of thermal radiation increases gradually with the laser power increases, which indicates that the melt pool temperature increases gradually with the heat input increases. Figure 17b shows the relationship between the three groups of melt pool dimensions and the intensity of the thermal radiation. Although the width is related to the thermal radiation intensity, the height and the penetration depth have little change as the thermal radiation intensity increases. It indicates that the width can be further controlled by varying the laser power to adjust the intensity of the thermal radiation. The results show that the width increases from 1.7 to 3 mm as the laser power increases from 1000 to 1700 W.

3 On-line monitoring of the quality

3.1 Microstructure

In the LAM process, the deviation between the actual value and the theoretical value of the element content in the melt pool is usually caused by the fluctuation of the carrier gas flow and the rotational speed of the powder feeder motor, while the content of elements in the forming part can greatly affect the microstructure and properties. Therefore, it is of great significance to control the element content in the melt pool in real time, which requires us to realize the on-line monitoring of element composition. At present, laser-induced breakdown spectroscopy (LIBS) is the main method for on-line monitoring of element composition.

Free calibration, calibration curve, and chemometrics are the commonly used quantitative analysis methods for LIBS. Among them, the relationship between spectral intensity and element content was established by the free calibration using the Boltzmann distribution [64], and the free calibration was successfully applied to the determination of solid samples [65–68]. Calibration curves were constructed by the calibration curve method based on the relationship between the spectral characteristics and the elemental concentrations

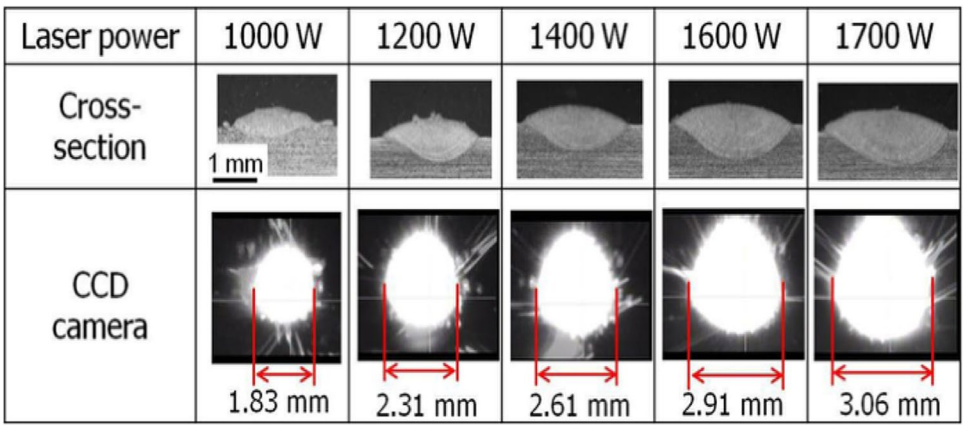

Fig. 16 Cross-sections of melt pool for different laser powers ($v = 10$ mm/s, $D_f = 36$ mm, $P_f = 0.01$ g/mm) [63]

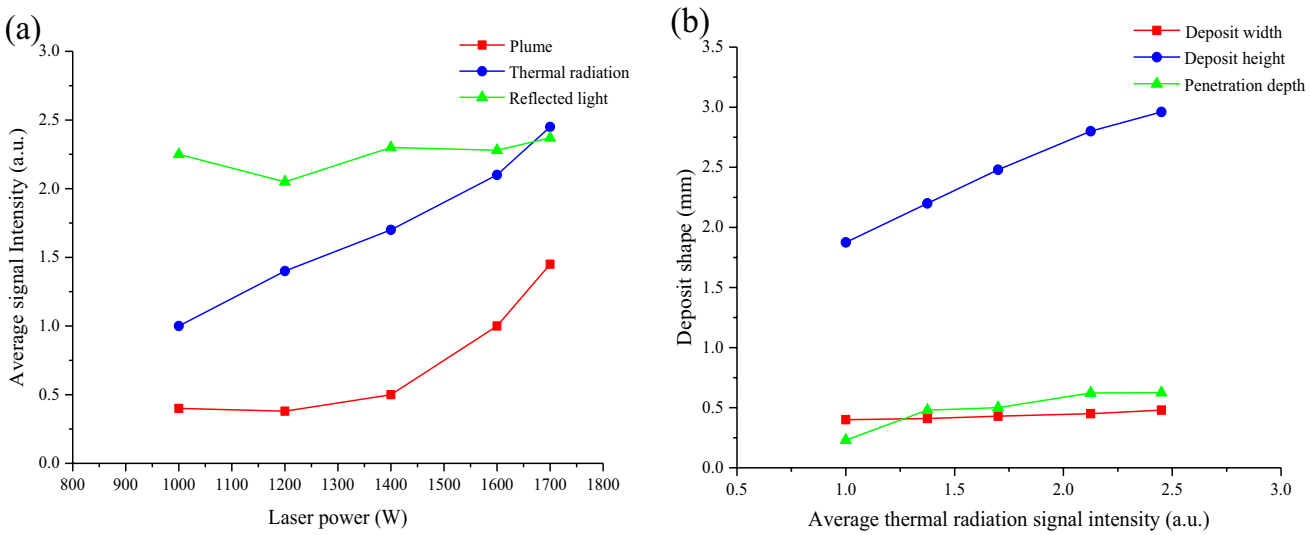

Fig. 17 Results of in-process monitoring ($v = 10$ mm/s, $D_f = 36$ mm, $P_f = 0.01$ g/mm): **a** relationship between signal intensity and laser power; **b** relationship between deposit shape and thermal radiation signal intensity [63]

[69]. The relationship between spectral characteristics and elemental concentrations was calculated by machine-learning algorithm, and the element composition prediction model was established by the chemometrics [70–74]. By means of the partial least squares method, Andrade et al. [70] quantified the element composition in brass samples, and the study found that the effect was better than the traditional calibration curve. At the same time, the accuracy of the artificial neural network algorithm for element composition [71] was investigated, which was superior to the calibration curve. Ayyalasomayajula et al. [72] found that the multiple linear regression calibration model was better than that of the single model. Sirven et al. [73] found that the monitoring accuracy of element composition was twice than that of the calibration curve by the artificial neural network algorithm. Through the combination of the neural network and the LIBS, Ferreira et al. [74] analyzed the copper in soil.

The feasibility of on-line quantitative analysis of multi-elements in LAM was demonstrated based on the LIBS. In order to estimate the influence of nickel enrichment on LIBS analysis, a series of samples with different WC powder feeding rates were prepared, and the LIBS was used to on-line measure the melt pool and the surface of the thermally solidified coating [75]. In order to remove the surface layer (about 200 μm), as a control experiment, some samples were grinded after cooling, and others were not grinded (Fig. 18a). It can be seen that the ungrinded sample has a lower concentration of WC particle compared with the grinded sample. EDX analysis clearly shows that the WC concentration on the ungrinded sample is 2 times lower than that after grinding (Fig. 18b), and the same results are obtained by XRF analysis. The on-line measurement of the melt pool and the surface of the thermally solidified coating by LIBS shows that the EDX and the XRF are relevant. Therefore, LIBS analysis can be performed within the melt pool to quantitatively analyze W and C.

During the synthesis of WC particle-reinforced Ni alloy wear-resistant coating, the quantitative chemical analysis of the element composition (Ni, W) was performed in real time by developing a compact LIBS probe and equipped with an industrial robot with a laser melting head. Due to the uneven distribution of WC particles on the coating surface, LIBS will be performed within the melt pool. In order to quantitatively estimate the influence of particle breakdown on LIBS plasma emission [76], the correlation analysis was carried out in the experiment (Fig. 19). Data for greater flow of WC particles are marked with pink color, while low concentration WC flows are shown with green color. It can be seen that the "reflected by particles" signal is positively correlated with the laser plasma emission indicating that the "off LIBS laser beam" spikes are caused by the particle reflection plasma emission. It is assumed that the laser ablation at powder particles will reduce the laser pulse energy that delivered to the melt pool surface. One can expect a negative correlation between these two signals. However, a positive correlation between laser plasma emission and "breakdown at particles" signals is observed for flows with different concentrations of WC. This indicates that "breakdown at particles" signal is partially due to the "reflection" rather than the micro plasmas formed on the particle surface.

By adjusting the temperature to adjust the scanning path of each laser, Nassar et al. [77] ensured that the temperature inside the deposited layer was within the set threshold, thus improving the forming quality and forming a uniform

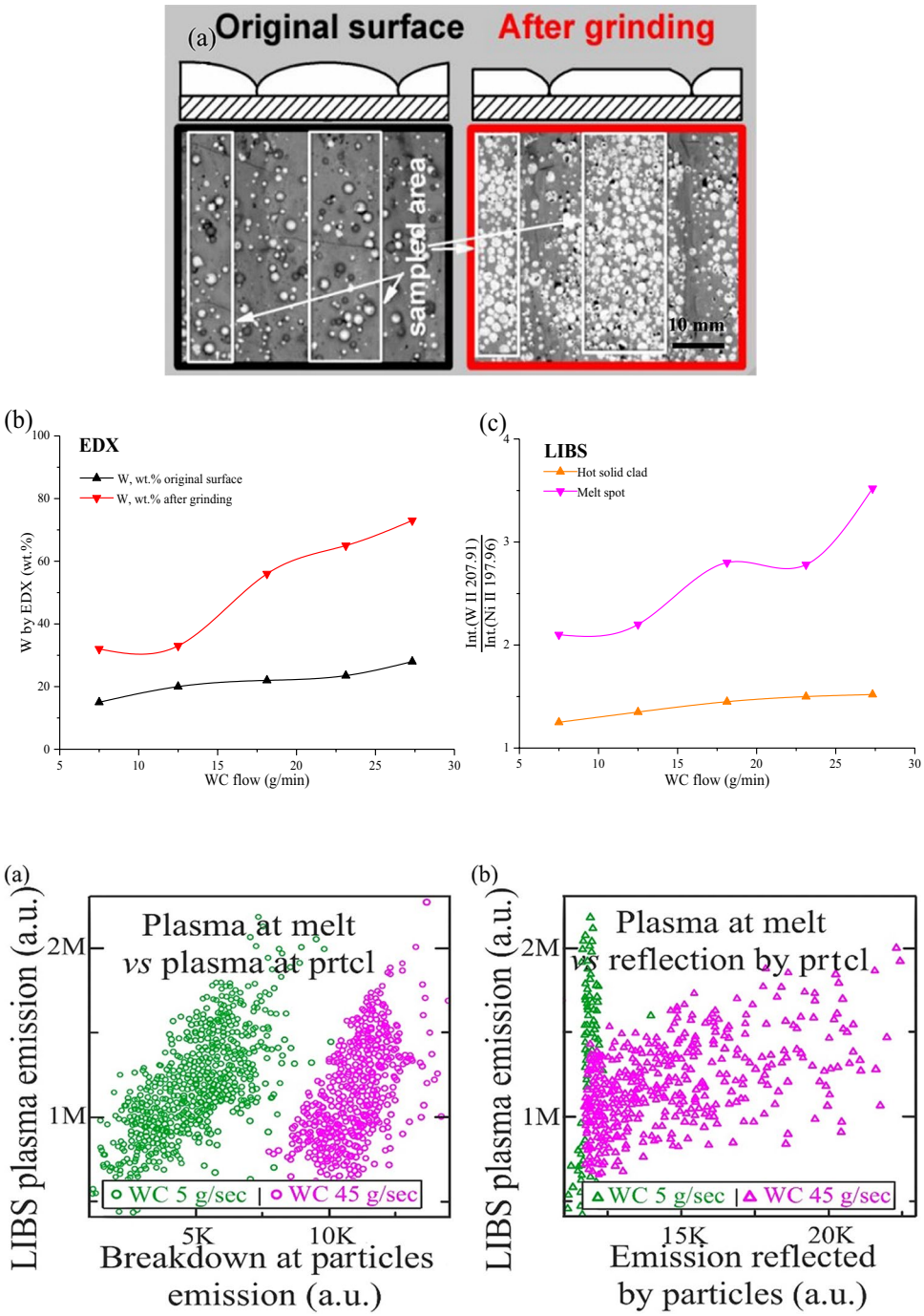

Fig. 18 Scanning electron microscopy images **a** of original (black) and ground (red) coating surfaces. Electron energy X-ray-dispersive (EDX) analysis results for tungsten **b** in case of virgin and ground surfaces. Laser-induced breakdown spectroscopy (LIBS) results for tungsten signals (ratio Int.(W II 207.91)/Int.(Ni II 208.57) in cases of melt bath (cyan) and hot-solidified clad (orange) sampling [75]

Fig. 19 Correlations of emission signals for the laser plasmas induced at melt pool surface and powder particles (**a**) and emission signals for laser plasma induced at melt surface and plasma light reflected by particle in flow (**b**) [76]

microstructure. By investigating the relationship between the spectral signal and the microstructure, Song et al. [78, 79] found that the changes in laser-induced plasma signal characteristics were caused by the changes in microstructure. When the samples with the same microstructure and different elements were scanned, the laser-induced spectral intensity ratio was linearly correlated with the element composition. When the samples with different microstructures and element compositions were scanned, the laser-induced spectral intensity ratio was nonlinearly correlated with the element composition. After the analysis of the microstructure, in order to monitor the change of Cr content inside the sample during laser deposition, the relationship between the fitting spectral intensity ratio, plasma temperature, and electron density and the Cr content was studied. Among them, the plasma temperature and electron density had little correlation with the Cr content, and the real-time monitoring of Cr content can be realized by fitting spectral intensity ratio. Figure 20 shows the predicted Cr percent by the fitting spectral intensity ratio [78]. According to the average

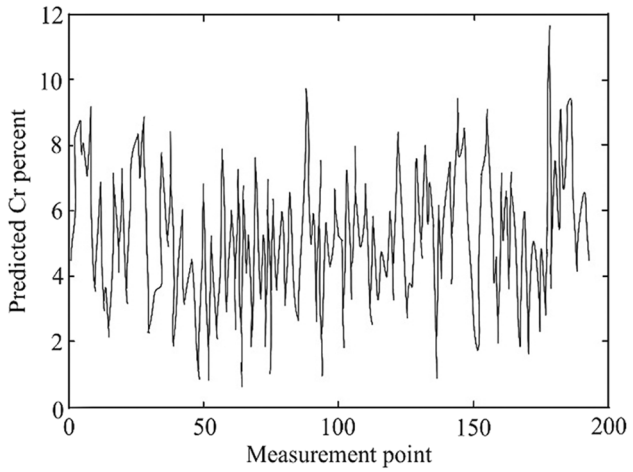

Fig. 20 Real-time chromium composition measured during direct metal deposition of alloyed H13 tool steel powder with certified Cr concentration of 5.27at.% [78]

predicted values of the four fitting spectral intensity ratios, the average content of Cr is 5.21%, the error is 0.06%, and the standard deviation is 4.28%.

During the synthesis of Fe and Ti, the composition of the elements was adjusted, and the corresponding plasma spectrum was monitored and analyzed [80]. Figure 21 shows the relationship between the four Fe-I/Ti-II line ratios and Ti weight percentage. We can observe that the line intensity ratio of the eutectic point is lower than the sides. At each side of the eutectic point, the Fe/Ti line ratios decrease with the decrease of Fe. Figure 22 shows the SEM morphology of Ti-Fe alloys with different compositions. The primary dendrite of TiFe phase with *B*2 CsCl structure is formed in hypereutectic alloy. The dendrite size decreases with the decrease of the Fe content. The hypoeutectic alloy is characterized by a small volume fraction of β-Ti + TiFe eutectic, which is distributed at the grain boundary of the β-Ti solid solution. The microstructure of the eutectic alloy is composed of fishbone β-Ti + TiFe eutectic with an average layer spacing of 0.6 μm. The dispersed TiFe (light color) phase is the dominant in the eutectic, and the β-Ti solid solution is formed between the TiFe eutectic phases.

3.2 Property

Through on-line preheating of the forming matrix surface, the temperature gradient can be reduced to a certain extent. At the same time, the thermal deformation and defects can be reduced, and the mechanical properties can be improved. In the LAM preheating process, the matrix preheating is the main method, and a few adopt the surface irradiation/radiation heating. However, the metal powders on the powder bed, forming the surface and matrix will change the chemical composition and cause segregation defects after excessive preheating. The temperature gradient is initially reduced by preheating, and then the temperature field on-line monitoring closed-loop feedback control system was used to reduce the temperature gradient and the growth direction of the parts, which cannot input different heat to different temperature gradient distribution areas, and only in this way can the mechanical properties be better controlled.

By preheating the matrix to 200–500 °C, Malý et al. [81] found that the increase in preheating temperature was linearly correlated with the reduction in thermal deformation, while preheating reduced the temperature gradient, thermal stress, and thermal deformation. The melting and solidification process of Ti powder was monitored by the X-ray synchrotron radiation. Sato et al. [82] found that there was a positive correlation between the preheating temperature and the surface smoothness when the Ti parts were formed by a matrix with different preheating temperatures. By preheating the formed substrate at high temperature, Ali et al. [83] found that when the formed matrix was preheated to 570 °C, the residual stresses were significantly reduced, and the strength and the ductility were significantly improved, which increased by 3.2% and 66.2%, respectively. By investigating the effect of substrate preheating temperature on the microstructure and residual stresses in 12CrNi2 alloy steel formed parts, Ding et al. [84] found that the matrix preheating reduced the residual stresses, and the increase of preheating temperature was accompanied by the decrease of martensite/bainite and the increase of ferrite. Kempen et al. [85] found that the preheating reduced the thermal stress, thermal deformation, cooling rate, and brittle martensite by comparing the matrix without preheating and with different preheating temperatures, which reduced the macroscopic cracking. Through preheating, Fallah et al. [86] found that the cracks in the coating were significantly reduced and the mechanical properties were greatly improved.

Stress variations within the material can affect the LAM process as well as the overall performance, so we need to control the stress variations through on-line monitoring techniques. Based on the temperature field, the residual stresses in the coating were accurately calculated by Zhang et al. [87] and Farahmand et al. [88]. Qi et al. [89] and Zhao et al. [90] accurately calculated the residual stress by introducing the phase transformation process into the calculation model, and combined with the parameters, and the residual stress study provided the data basis for the subsequent post-processing test. By means of neutron diffraction, Moat et al. [91] and Pratt et al. [92] measured the residual stress distribution of Ni-based high-temperature alloy samples. Oliveira et al. [93] measured the residual stresses within the Co-based coating by X-ray diffraction (XRD). However, neither mathematical simulation nor back testing can achieve the purpose of repairing parts.

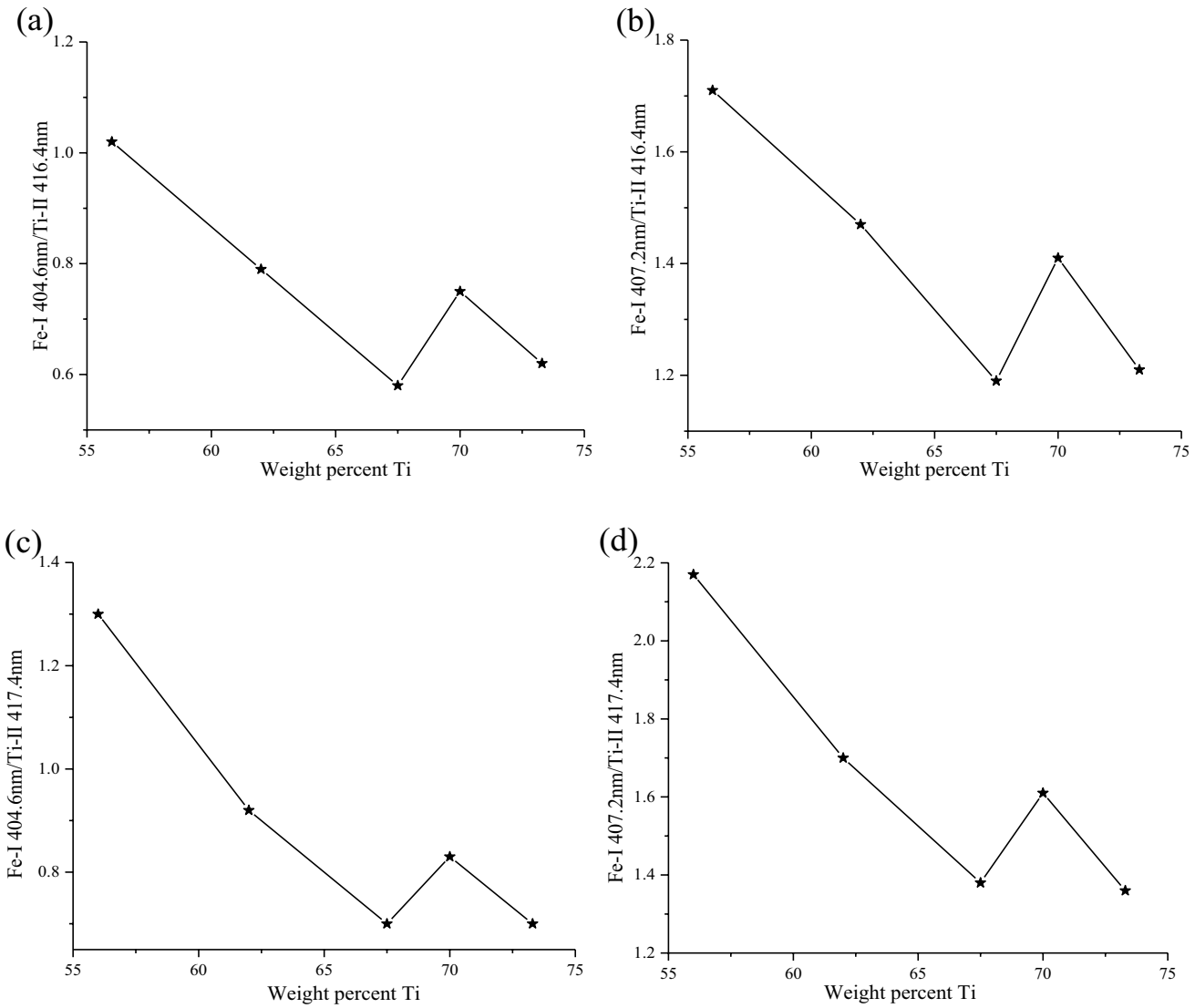

Fig. 21 Relationship between the four Fe-I/Ti-II line ratios and Ti weight percentage. **a** Fe-I 404.6 nm/Ti-II 416.4 nm; **b** Fe-I 407.2 nm/Ti-II 416.4 nm; **c** Fe-I 404.6 nm/Ti-II 417.4 nm; **d** Fe-I 407.2 nm/Ti-II 417.4 nm [80]

The indirect measurement to reflect the state of the deposition layer by on-line monitoring the residual stress changes in the back of the matrix has become the main method of on-line monitoring residual stress. By linear variable differential transformer (LVDT), Andreas et al. [94] measured the deformation in the central region at the back of the matrix, but it cannot directly reflect the changes inside the deposited layer. Biegler et al. [95] measured the variation of the residual stress at the bottom of the matrix by digital image correlation (DIC). This method has a large measurement range, and it can more intuitively reflect the residual stress change than LVDT. However, due to the continuous change of material shape and solid–liquid interface, the residual stress inside the deposited layer cannot be measured by this method. Therefore, the further research is needed for on-line monitoring of residual stresses inside the deposited layer.

Firstly, the matrix was preheated at 1050 °C to obtain the crack-free sample, and then the tensile test of the laser deposited sample was carried out at room temperature [96]. The results are shown in Table 4. It is found that the yield strength (YS) and ultimate tensile strength (UTS) are 14% and 44% higher than those of other studies [97], and the elongation (EL) is 44% higher.

Figure 23 shows the fracture surface of the specimen. It can be seen that the crack initiates near the fracture surface, and the shear lip area is small, as shown in Fig. 23a. In the radial region (Fig. 23b), dendrites with dimple pattern appear, indicating that the fracture preferentially occurs between dendrites and is a ductile fracture. It can be seen

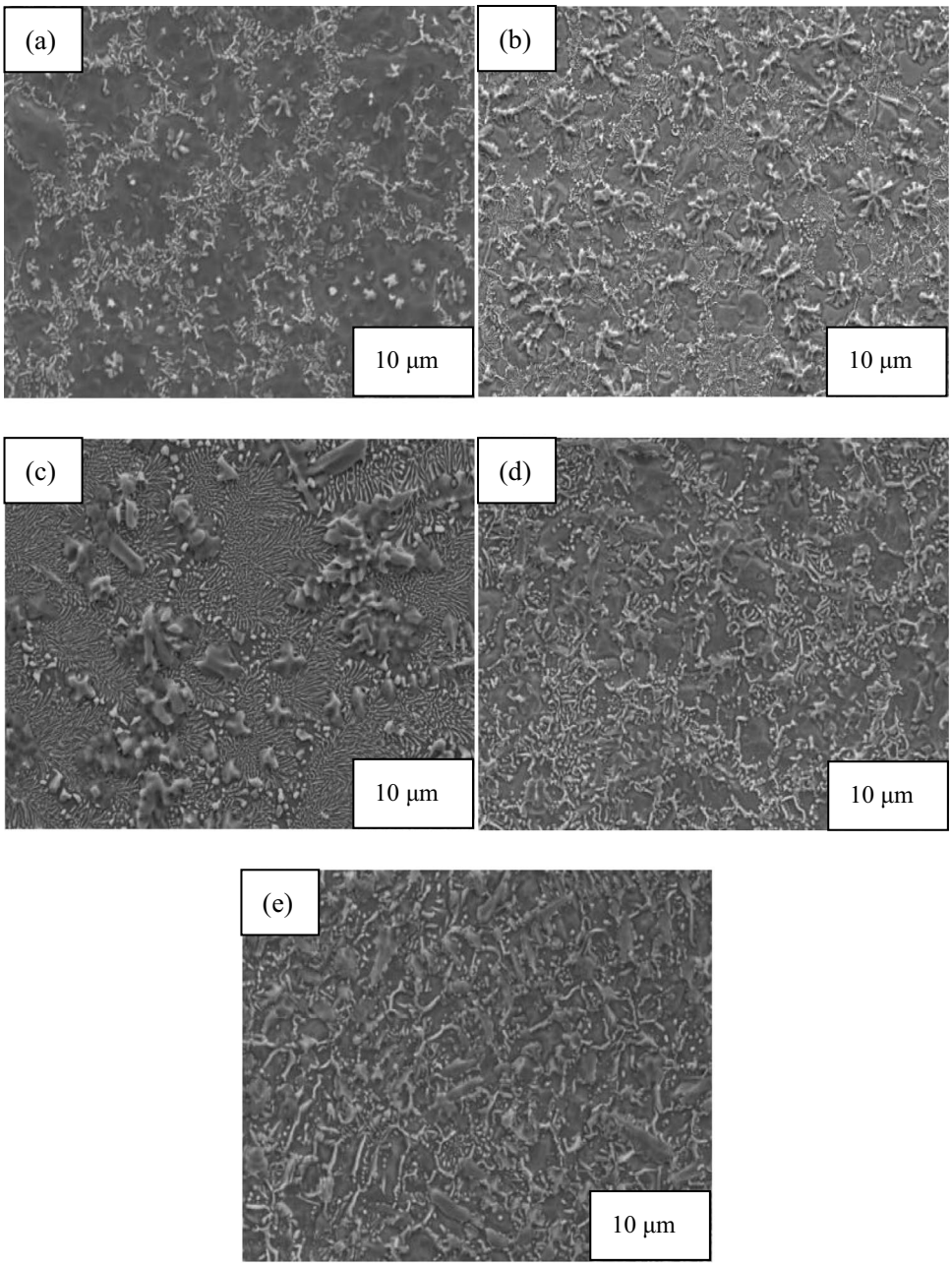

Fig. 22 SEM morphology of the Ti-Fe alloys. **a** $Ti_{73}Fe_{27}$ alloy; **b** $Ti_{70}Fe_{30}$ alloy; **c** $Ti_{67.5}Fe_{32.5}$ alloy; **d** $Ti_{62}Fe_{38}$ alloy; and **e** $Ti_{56}Fe_{44}$ alloy [80]

Table 4 Tensile properties of LSF Inconel 738LC alloy at room temperature [96]

Sample	YS (MPa)	UTS (MPa)	EL (%)
As-deposited	871	1074	10.8
Cast reference [48]	765	945	7.5

from the high-magnification morphology (Fig. 23c) that there are massive particles in the pits, which are (Ti,Ta)C carbides analyzed by EDS. The large-sized carbides are not conducive to the increase of elongation, while the size of block carbides is less than 1 μm, so the elongation is improved.

Figure 24 shows the microhardness of the specimens. It can be seen that the average microhardness preheated at 800 °C, 900 °C, and without is approximately the same. And the average microhardness preheated at 1050 °C is lower than that of the others. In particular, at 1050 °C, the average microhardness regularly increases from bottom to top, while the microhardness of the other specimens has no significant difference along the height direction. This indicates that the higher temperature preheating affects the correlation between the microcosmic phases and the main

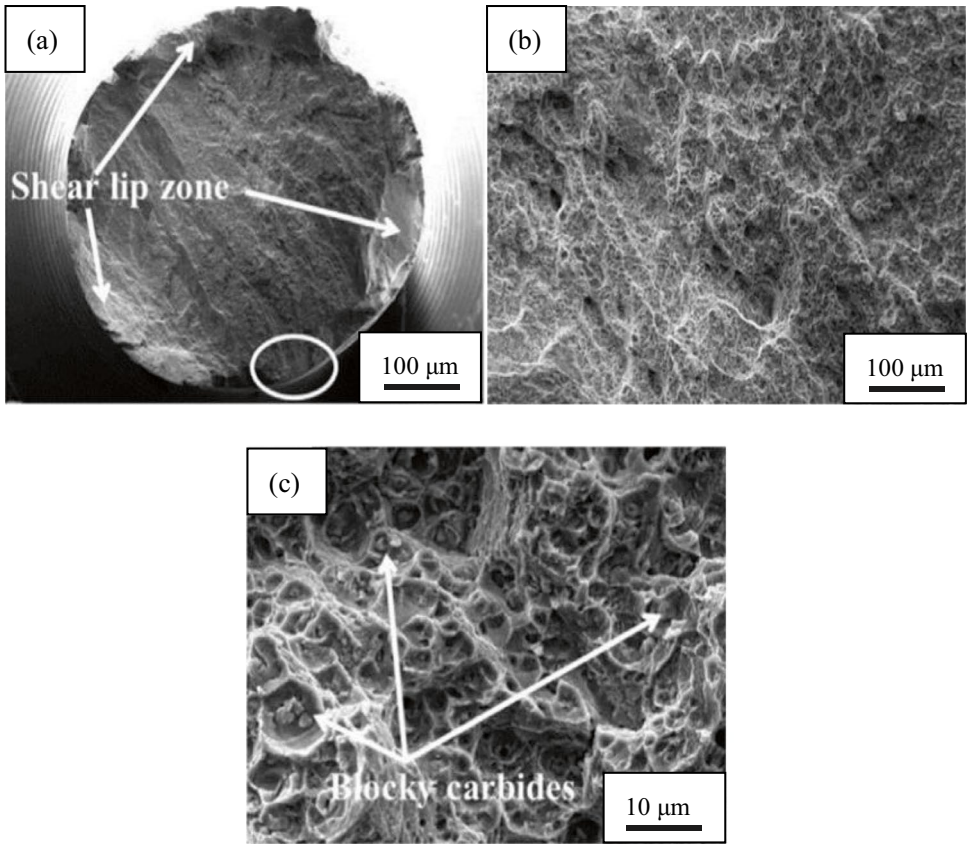

Fig. 23 Fracture surface **a** radial region; **b** dimple pattern in radial region; **c** of LSF IN-738LC alloy [96]

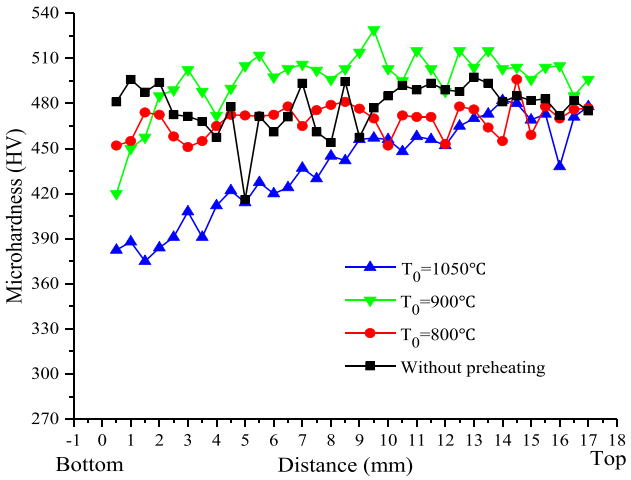

Fig. 24 Microhardness of the LSF IN-738LC samples under different preheating conditions [96]

reinforcement phase of the matrix, resulting in the decrease of the microhardness.

Through the above analysis, we can design an on-line monitoring system for LAM based on multi-source information control system. As shown in Fig. 25, the advanced algorithms, including machine learning, deep learning, digital twinning, and cloud data processing, work together with the new monitoring technologies, including laser ultrasonic (LU), X-ray computed tomography (XCT), and X-ray backscatter imaging (XBT). By establishing an on-line monitoring system for LAM based on multi-source information control system, we can study the non-equilibrium rapid solidification behavior and heat exchange mechanism of the molten pool under multiple process parameters; explore the behavior essence of heat transfer, convection, and other phenomena in the molten pool under the condition of heat exchange; carry out the application research of on-line monitoring and control methods for different LAM processes; and establish an on-line regulation model between various process parameters and molten pool information, which is to realize the process monitoring and adaptive control of the melt pool temperature, melt pool morphology, melt pool dimensions, microstructure, properties, and dimensional accuracy of parts. The designed LAM on-line monitoring system can get personalized manufacturing parts, improve the properties of the parts, and meet the subsequent production and conditions.

4 Conclusions

The summary and analysis of the on-line monitoring technology of LAM can effectively detect the defects, improve the forming quality by real-time regulating the process

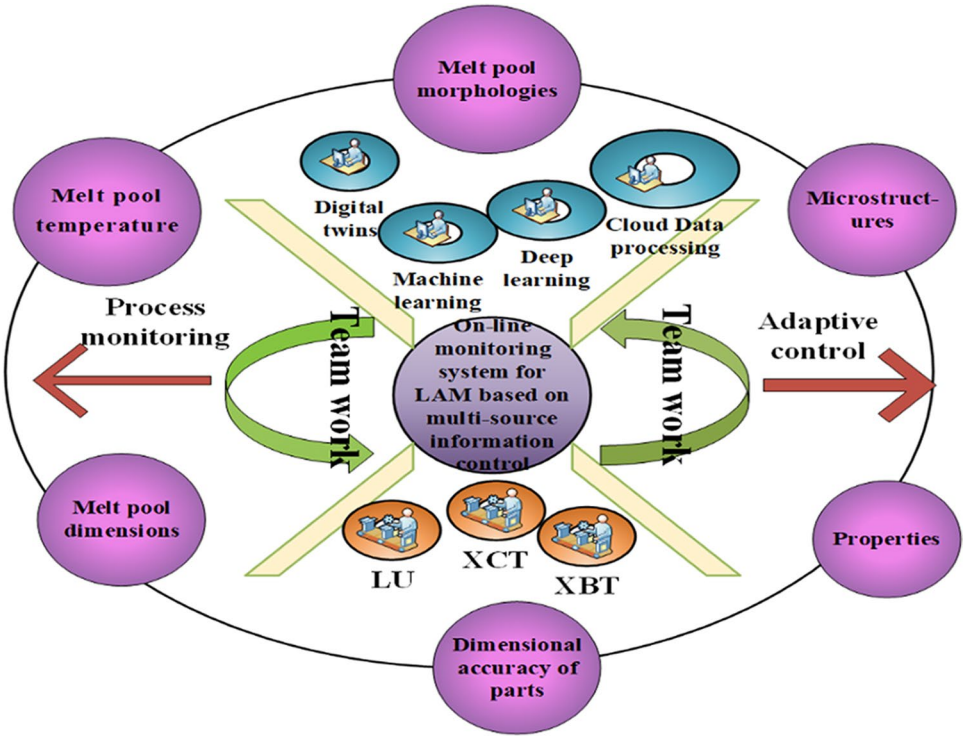

Fig. 25 Frame diagram of on-line monitoring system for LAM based on multi-source information control

parameters, and eliminate the restrictions on the development caused by various process defects. Future on-line monitoring techniques should focus on the following:

(1) The monitoring tools commonly used in LAM have limitations in accuracy and response time, and the monitored sample information is limited. In the process of data processing, only to ensure the joint improvement of software and hardware can a large number of measured data be quickly analyzed, and it is also an important method to ensure the real-time of on-line monitoring system. Therefore, we need to develop the new on-line monitoring tools and new on-line monitoring technologies, develop special technologies that are suitable for LAM, and establish accurate correspondence between the defects and the signals. Thus, some new monitoring techniques such as laser ultrasound (LU), X-ray computed tomography (XCT), and X-ray backscatter imaging (XBT) have greater application potential in on-line monitoring. Although these new monitoring techniques are more difficult to integrate into LAM on-line monitoring systems, they can measure more information inside the sample. The integrated and collaborative research of software in LAM and on-line monitoring will become an important research direction of LAM on-line monitoring technology in the future.
(2) In the LAM process, a variety of defects are generated, and a single monitoring technology can only accurately monitor one type of defect, so we need to make multiple monitoring technologies work together to establish an integrated on-line monitoring system. The internal defects of LAM parts are the most critical to the forming quality, but there are few studies on the on-line monitoring. Therefore, the on-line monitoring will become the key breakthrough direction of future detection technology.
(3) The algorithms are the core of the closed-loop feedback control system and the data processing. PI and PID control algorithms are commonly used in on-line monitoring technology, and algorithms such as SVR, ANNs, and PLSR can also be applied to data processing. With the development of big data and artificial intelligence, we can combine the advanced algorithms such as neural network, machine learning, deep learning, digital twinning, and cloud data processing with the LAM on-line monitoring process and create the new development vitality. This is also a hot research direction of LAM on-line monitoring technology in the future.

Funding This research work was supported by the National Natural Science Foundation of China (Grant No. 52175455), the Science and Technology Innovation Fund of Dalian (Grant No. 2020JJ26GX040), Fundamental Research Funds for the Central Universities, the Guangdong Provincial University Innovation Team Project (Grant No.

2020KCXTD012), and the 2020 Li Ka Shing Foundation Cross-Disciplinary Research (Grant No. 2020LKSFG01D).

Data availability TransparenT.

Code availability Not applicable.

Declarations

Conflict of interest The authors declare no competing interests.

References

1. Hoye N, Li HJ, Cuiuri D, Paradowska A (2014) Measurement of residual stresses in titanium aerospace components formed via additive manufacturing. Mater Sci Forum 777:124–129. https://doi.org/10.4028/www.scientific.net/MSF.777.124
2. Salmi M, Paloheimo KS, Tuomi J, Wolff J, Mäkitie A (2013) Accuracy of medical models made by additive manufacturing (rapid manufacturing). J Cranio-Maxillo-Fac Surg 41:603–609. https://doi.org/10.1016/j.jcms.2012.11.041
3. Campbell I, Bourell D, Gibson I (2012) Additive manufacturing: rapid prototyping comes of age. Rapid Prototyp J 18:255–258. https://doi.org/10.1108/13552541211231563
4. Ngo TD, Kashani A, Imbalzano G, Nguyen KTQ, Hui D (2018) Additive manufacturing (3D printing):a review of materials, methods, applications and challenges. Compos B Eng 143:172–196. https://doi.org/10.1016/j.compositesb.2018.02.012
5. Murr LE (2018) A metallographic review of 3D printing/additive manufacturing of metal and alloy products and components. Metallogr Microstruct Anal 7:103–132. https://doi.org/10.1007/s13632-018-0433-6
6. Cao L, Chen SY, Wei MW, Guo Q, Liang J, Liu CS, Wang M (2019) Effect of laser energy density on defects behavior of direct laser depositing 24CrNiMo alloy steel. Opt Laser Technol 111:541–553. https://doi.org/10.1016/j.optlastec.2018.10.025
7. Liu QC, Elambasseril J, Sun SJ, Leary M, Brandt M, Sharp PK (2014) The effect of manufacturing defects on the fatigue behaviour of Ti-6Al-4V specimens fabricated using selective laser melting. Adv Mat Res 891(892):1519–1524. https://doi.org/10.4028/www.scientific.net/AMR.891-892.1519
8. Gong HJ, Rafi K, Gu HF, Ram GDJ, Starr T, Stucker B (2015) Influence of defects on mechanical properties of Ti-6Al-4V components produced by selective laser melting and electron beam melting. Mater Des 86:545–554. https://doi.org/10.1016/j.matdes.2015.07.147
9. Xie RD, Li DC, Cui B, Zhang LZ, Gao F (2018) A defects detection method based on infrared scanning in laser metal deposition process. Rapid Prototyp J 24:945–954. https://doi.org/10.1108/RPJ-04-2017-0053
10. Liu WW, Saleheen KM, Tang ZJ, Wang H, Al-Hammadi G, Abdelrahman A, Zhao YX, Hua SG, Wang FT (2021) Review on scanning pattern evaluation in laser-based additive manufacturing. Opt Eng 60:070901. https://doi.org/10.1117/1.OE.60.7.070901
11. Heralić A, Christiansson AK, Ottosson M, Lennartson B (2010) Increased stability in laser metal wire deposition through feedback from optical measurements. Opt Lasers Eng 48:478–485. https://doi.org/10.1016/j.optlaseng.2009.08.012
12. Hofman JT, Pathiraj B, Dijk J, Lange DF, Meijer J (2012) A camera based feedback control strategy for the laser cladding process. J Mater Process Technol 212:2455–2462. https://doi.org/10.1016/j.jmatprotec.2012.06.027
13. Li JS, Vijayavel BS, Bhaskar D, Jyoti M (2012) Control of melt pool temperature and deposition height during direct metal deposition process. Int J Adv Manuf Technol 58:247–256. https://doi.org/10.1007/s00170-011-3395-2
14. Arias JL, Montealegre MA, Vidal F, Rodríguez J, Mann S, Abels P, Motmans F Real-time laser cladding control with variable spot size. In: Laser 3D Manufacturing, San Francisco, CA, 2014. SPIE. https://doi.org/10.1117/12.2040058
15. Kanko JA, Sibley AP, Fraser JM (2016) In situ morphology-based defect detection of selective laser melting through inline coherent imaging. J Mater Process Technol 231:488–500. https://doi.org/10.1016/j.jmatprotec.2015.12.024
16. Tang L, Landers RG (2011) Layer-to-layer height control for laser metal deposition process. J Manuf Sci Eng 133:021009. https://doi.org/10.1115/1.4003691
17. Barua S, Liou F, Newkirk J, Sparks T (2014) Vision-based defect detection in laser metal deposition process. Rapid Prototyp J 20:77–85. https://doi.org/10.1108/RPJ-04-2012-0036
18. Tan H, Chen J, Lin X, Zhang FY, Huang WD (2008) Research on molten pool temperature in the process of laser rapid forming. J Mater Process Technol 198:454–462. https://doi.org/10.1016/j.jmatprotec.2007.06.090
19. Hu YP, Chen CW, Mukherjee K (2000) Measurement of temperature distributions during laser cladding process. J Laser Appl 12:126–130. https://doi.org/10.2351/1.521921
20. Lin J, Steen WM (1998) An in-process method for the inverse estimation of the powder catchment efficiency during laser cladding. Opt Laser Technol 30:77–84. https://doi.org/10.1016/S0030-3992(98)00007-3
21. Li L, Steen WM, Hibberd RD, Brookfield DJ In-process clad quality monitoring using optical method. In: Laser Assisted Processing, The Hague, Netherlands, 1990. SPIE. https://doi.org/10.1117/12.20624
22. Song LJ, Mazumder J (2010) Feedback control of melt pool temperature during laser cladding process. IEEE Trans Control Syst Technol 19:1349–1356. https://doi.org/10.1109/TCST.2010.2093901
23. Pavlov M, Novichenko D, Doubenskaia (2011) Optical diagnostics of deposition of metal matrix composites by laser cladding. Phys Procedia 12:674–682. https://doi.org/10.1016/j.phpro.2011.03.084
24. Hu D, Kovacevic R (2003) Modelling and measuring the thermal behaviour of the molten pool in closed-loop controlled laser-based additive manufacturing. Proc Instn Mech Engrs Part B: J Engineering Manufacture 217:441–452. https://doi.org/10.1243/095440503321628125
25. Hu DM, Kovacevic R (2003) Sensing, modeling and control for laser-based additive manufacturing. Int J Mach Tool Manufact 43:51–60. https://doi.org/10.1016/S0890-6955(02)00163-3
26. Scharun M, Fricke-Begemann C, Noll R (2013) Laser-induced breakdown spectroscopy with multi-kHz fibre laser for mobile metal analysis tasks-a comparison of different analysis methods and with a mobile spark-discharge optical emission spectroscopy apparatus. Spectrochim Acta Part B 87:198–207. https://doi.org/10.1016/j.sab.2013.05.007
27. Abdellatif G, Imam H (2002) A study of the laser plasma parameters at different laser wavelengths. Spectrochim Acta Part B 57:1155–1165. https://doi.org/10.1016/S0584-8547(02)00057-5
28. Barnett C, Cahoon E, Almirall JR (2008) Wavelength dependence on the elemental analysis of glass by laser induced breakdown spectroscopy. Spectrochim Acta Part B 63:1016–1023. https://doi.org/10.1016/j.sab.2008.07.002
29. Fornarini L, Spizzichino V, Colao F, Fantoni R, Lazic V (2006) Influence of laser wavelength on LIBS diagnostics applied to the analysis of ancient bronzes. Anal Bioanal Chem 385:272–280. https://doi.org/10.1007/s00216-006-0300-1

30. Lu QY, Wong CH (2018) Additive manufacturing process monitoring and control by non-destructive testing techniques: challenges and in-process monitoring. Virtual Phys Prototy 13:39–48. https://doi.org/10.1080/17452759.2017.1351201
31. Shin J, Mazumder J (2018) Composition monitoring using plasma diagnostics during direct metal deposition (DMD) process. Opt Laser Technol 106:40–46. https://doi.org/10.1016/j.optlastec.2018.03.020
32. Plotnikov Y, Henkel D, Burdick J, French A, Sions J, Bourne K (2019) Infrared-assisted acoustic emission process monitoring for additive manufacturing. In: AIP Conference Proceedings, vol. 2102, no. May. https://doi.org/10.1063/1.5099710
33. Lee YS, Kirka MM, Ferguson J, Paquit VC (2020) Correlations of cracking with scan strategy and build geometry in electron beam powder bed additive manufacturing. Addit Manuf 32:101031. https://doi.org/10.1016/j.addma.2019.101031
34. Gaja H, Liou F (2017) Defects monitoring of laser metal deposition using acoustic emission sensor. Int J Adv Manuf Technol 90:561–574. https://doi.org/10.1007/s00170-016-9366-x
35. Kouprianoff D, Luwes N, Newby E, Yadroitsava I, Yadroitsev I (2017) On-line monitoring of laser powder bed fusion by acoustic emission: acoustic emission for inspection of single tracks under different powder layer thickness. In: 2017 Pattern Recognition Association of South Africa and Robotics and Mechatronics (PRASA-RobMech), https://doi.org/10.1109/RoboMech.2017.8261148
36. Shevchik SA, Kenel C, Leinenbach C, Wasmer K (2018) Acoustic emission for in-situ quality monitoring in additive manufacturing using spectral convolutional neural networks. Addit Manuf 21:598–604. https://doi.org/10.1016/j.addma.2017.11.012
37. Cerniglia D, Scafidi M, Pantano A, Rudlin J (2015) Inspection of additive manufactured layered components. Ultrasonics 62:292–298. https://doi.org/10.1016/j.ultras.2015.06.001
38. Arısoy YM, Criales LE, Özel T (2019) Modeling and simulation of thermal field and solidification in laser powder bed fusion of nickel alloy IN625. Opt Laser Technol 109:278–292. https://doi.org/10.1016/j.optlastec.2018.08.016
39. Yin J, Peng GY, Chen CP, Yang JJ, Zhu HH, Ke LD, Wang ZM, Wang DZ, Ma MM, Wang GQ, Zeng XY (2018) Thermal behavior and grain growth orientation during selective laser melting of Ti-6Al-4V alloy. J Mater Process Technol 260:57–65. https://doi.org/10.1016/j.jmatprotec.2018.04.035
40. Schänzel M, Shakirov D, Ilin A, Ploshikhin V (2019) Coupled thermo-mechanical process simulation method for selective laser melting considering phase transformation steels. Comput Math Appl 78:2230–2246. https://doi.org/10.1016/j.camwa.2019.01.019
41. Panda BK, Sahoo S (2019) Thermo-mechanical modeling and validation of stress field during laser powder bed fusion of AlSi10Mg built part. Results Phys 12:1372–1381. https://doi.org/10.1016/j.rinp.2019.01.002
42. Wei P, Wei ZY, Chen Z, He YY, Du J (2017) Thermal behavior in single track during selective laser melting of AlSi10Mg powder. Appl Phys A 123:604. https://doi.org/10.1007/s00339-017-1194-9
43. Tan H, Chen J, Zhang FY, Lin X, Huang WD (2010) Estimation of laser solid forming process based on temperature measurement. Opt Laser Technol 42:47–54. https://doi.org/10.1016/j.optlastec.2009.04.016
44. Bi GJ, Gasser A, Wissenbach K, Drenker A, Poprawe R (2006) Characterization of the process control for the direct laser metallic powder deposition. Surf Coat Technol 201:2676–2683. https://doi.org/10.1016/j.surfcoat.2006.05.006
45. Tang L, Landers RG (2010) Melt pool temperature control for laser metal deposition processes-part II: layer-to-layer temperature control. J Manuf Sci Eng 132:011011. https://doi.org/10.1115/1.4000883
46. Salehi D, Brandt M (2006) Melt pool temperature control using LabVIEW in Nd:YAG laser blown powder cladding process. Int J Adv Manuf Technol 29:273–278. https://doi.org/10.1007/s00170-005-2514-3
47. Devesse W, Baere DD, Hinderdael M, Guillaume P (2016) Hardware-in-the-loop control of additive manufacturing processes using temperature feedback. J Laser Appl 28:022302. https://doi.org/10.2351/1.4943911
48. Song LJ, Singh VB, Dutta B, Mazumder J (2012) Control of melt pool temperature and deposition height during direct metal deposition process. Int J Adv Manuf Technol 58:247–256. https://doi.org/10.1007/s00170-011-3395-2
49. Tang L, Landers RG (2010) Melt pool temperature control for laser metal deposition processes-part I: online temperature control. J Manuf Sci Eng 132:011010. https://doi.org/10.1115/1.4000882
50. Asselin M, Toyserkani E, Iravani-Tabrizipour M, Khajepour A (2005) Development of trinocular CCD-based optical detector for real-time monitoring of laser cladding. IEEE ASME Int Conf Adv Intell Mechatron 3:1190–1196. https://doi.org/10.1109/ICMA.2005.1626722
51. Song LJ, Wang FH, Li SM, Han X (2017) Phase congruency melt pool edge extraction for laser additive manufacturing. J Mater Process Technol 250:261–269. https://doi.org/10.1016/j.jmatprotec.2017.07.013
52. Fathi A, Khajepour A, Durali M, Toyserkani E (2008) Geometry control of the deposited layer in a nonplanar laser cladding process using a variable structure controller. J Manuf Sci Eng 130:031003. https://doi.org/10.1115/1.2823085
53. Zeinali M, Khajepour A (2010) Height control in laser cladding using adaptive sliding mode technique: theory and experiment. J Manuf Sci Eng 132:041016. https://doi.org/10.1115/1.4002023
54. Moralejo S, Penaranda X, Nieto S, Barrios A, Arrizubieta I, Tabernero I, Figueras J (2017) A feedforward controller for tuning laser cladding melt pool geometry in real time. Int J Adv Manuf Technol 89:821–831. https://doi.org/10.1007/s00170-016-9138-7
55. Yang Q (2019) Study of size detection and control of molten pool during laser cladding. Hefei University of Technology. Hefei, China. https://kns.cnki.net/kcms/detail/detail.aspx?FileName=1019218904.nh&DbName=CMFD2019
56. Ocylok S, Alexeev E, Mann S, Weisheit A, Wissenbach K, Kelbassa I (2014) Correlation of melt pool geometry and process parameters during laser metal deposition by coaxial process monitoring. Phys Procedia 56:228–238. https://doi.org/10.1016/j.phpro.2014.08.167
57. Tabernero I, Lamikiz A, Martínez S, Ukar E, López De Lacalle LN (2012) Geometric modelling of added layers by coaxial laser cladding. Phys Procedia 39:913–920. https://doi.org/10.1016/j.phpro.2012.10.116
58. Ding YY, Warton J, Kovacevic R (2016) Development of sensing and control system for robotized laser-based direct metal addition system. Addit Manuf 10:24–35. https://doi.org/10.1016/j.addma.2016.01.002
59. Qin LY, Xu LL, Yang G, Liu Q, Wang W (2018) Analysis and prediction of melt pool size in laser deposition manufacturing. Infrared Laser Eng 47:80–86. https://doi.org/10.3788/IRLA201847.1106009
60. Mutabue T, Colin C, Malot T, Aubry P (2004) Influence of process monitoring devices on direct manufacturing by laser cladding for aeronautic components. In: International Congress on Applications of Lasers & Electro-Optics, vol. 2004, no. 1. https://doi.org/10.2351/1.5060184
61. Bi GJ, Gasser A, Wissenbach K, Drenker A, Poprawe R (2006) Identification and qualification of temperature signal for monitoring and control in laser cladding. Opt Lasers Eng 44:1348–1359. https://doi.org/10.1016/j.optlaseng.2006.01.009

62. Craeghs T, Bechmann F, Berumen S, Kruth JP (2010) Feedback control of layer wise laser melting using optical sensors. Phys Procedia 5:505–514. https://doi.org/10.1016/j.phpro.2010.08.078
63. Miyagi M, Tsukamoto T, Kawanaka H (2014) Adaptive shape control of laser-deposited metal structures by adjusting weld pool size. J Laser Appl 26:032003. https://doi.org/10.2351/1.4869499
64. Ciucci A, Corsi M, Palleschi V, Rastelli S, Salvetti A, Tognoni E (1999) New procedure for quantitative elemental analysis by laser-induced plasma spectroscopy. Appl Spectrosc 53:960–964. https://doi.org/10.1366/0003702991947612
65. Zhu XQ, Xu T, Lin QY, Liang L, Niu GH, Lai HJ, Xu MJ, Wang X, Li H, Duan YX (2014) Advanced statistical analysis of laser-induced breakdown spectroscopy data to discriminate sedimentary rocks based on Czerny-Turner and Echelle spectrometers. Spectrochim Acta Part B 93:8–13. https://doi.org/10.1016/j.sab.2014.01.001
66. Tognoni E, Cristoforetti G, Legnaioli S, Palleschi V (2010) Calibration-free laser-induced breakdown spectroscopy: state of the art. Spectrochim Acta Part B 65:1–14. https://doi.org/10.1016/j.sab.2009.11.006
67. Herrera KK, Tognoni E, Omenetto N, Smitha BW, Winefordner JD (2009) Semi-quantitative analysis of metal alloys, brass and soil samples by calibration-free laser-induced breakdown spectroscopy: recent results and considerations. J Anal At Spectrom 24:413–425. https://doi.org/10.1039/B820493D
68. Tognoni E, Cristoforetti G, Legnaioli S, Palleschi V, Salvetti A, Mueller M, Panne U, Gornushkin I (2007) A numerical study of expected accuracy and precision in calibration-free laser-induced breakdown spectroscopy in the assumption of ideal analytical plasma. Spectrochim Acta Part B 62:1287–1302. https://doi.org/10.1016/j.sab.2007.10.005
69. Cabalín L, Romero D, García CC, Baena J, Laserna J (2002) Time-resolved laser-induced plasma spectrometry for determination of minor elements in steelmaking process samples. Anal Bioanal Chem 372:352–359. https://doi.org/10.1007/s00216-001-1121-x
70. Andrade JM, Cristoforetti G, Legnaioli S, Lorenzetti G, Palleschi V, Shaltout AA (2010) Classical univariate calibration and partial least squares for quantitative analysis of brass samples by laser-induced breakdown spectroscopy. Spectrochim Acta Part B 65:658–663. https://doi.org/10.1016/j.sab.2010.04.008
71. Andrea ED, Pagnotta S, Grifoni E, Lorenzetti G, Legnaioli S, Palleschi V, Lazzerini B (2014) An artificial neural network approach to laser-induced breakdown spectroscopy quantitative analysis. Spectrochim Acta Part B 99:52–58. https://doi.org/10.1016/j.sab.2014.06.012
72. Ayyalasomayajula KK, Yu-Yueh F, Singh JP, McIntyre DL, Jain J (2012) Application of laser-induced breakdown spectroscopy for total carbon quantification in soil samples. Appl Opt 51:149–154. https://doi.org/10.1364/AO.51.00B149
73. Sirven JB, Bousquet B, Canioni L, Sarger L (2006) Laser-induced breakdown spectroscopy of composite samples: comparison of advanced chemometrics methods. Anal Chem 78:1462–1469. https://doi.org/10.1021/ac051721p
74. Ferreira EC, Milori DMBP, Ferreira EJ, Silva RMD, Martin-Neto L (2008) Artificial neural network for Cu quantitative determination in soil using a portable laser induced breakdown spectroscopy system. Spectrochim Acta Part B 63:1216–1220. https://doi.org/10.1016/j.sab.2008.08.016
75. Lednev VN, Sdvizhenskii PA, Asyutin RD, Tretyakov RS, Grishin MY, Stavertiy AY, Pershin SM (2019) In situ multi-elemental analysis by laser induced breakdown spectroscopy in additive manufacturing. Addit Manuf 25:64–70. https://doi.org/10.1016/j.addma.2018.10.043
76. Lednev VN, Sdvizhenskii PA, Asyutin RD, Tretyakov RS, Grishin MY, Stavertiy AY, Fedorov AN, Pershin SM (2019) In situ elemental analysis and failures detection during additive manufacturing process utilizing laser induced breakdown spectroscopy. Opt Express 27:4612–4628. https://doi.org/10.1364/OE.27.004612
77. Nassar AR, Keist JS, Reutzel EW, Spurgeon TJ (2015) Intra-layer closed-loop control of build plan during directed energy additive manufacturing of Ti-6Al-4V. Addi Manuf 6:39–52. https://doi.org/10.1016/j.addma.2015.03.005
78. Song LJ, Mazumder J (2012) Real time Cr measurement using optical emission spectroscopy during direct metal deposition process. IEEE Sensors J 12:958–964. https://doi.org/10.1109/JSEN.2011.2162316
79. Song LJ, Huang WK, Han X, Mazumder J (2017) Real-time composition monitoring using support vector regression of laser-induced plasma for laser additive manufacturing. IEEE Trans Ind Electron 64:633–642. https://doi.org/10.1109/TIE.2016.2608318
80. Song LJ, Wang CS, Mazumder J (2012) Identification of phase transformation using optical emission spectroscopy for direct metal deposition process. In: High Power Laser Mater Processing Laser Beam Delivery Diagnostics Applications, San Francisco, CA, SPIE. https://doi.org/10.1117/12.908264
81. Malý M, Höller C, Skalon M, Meier B, Koutný D, Pichler R, Sommitsch C, Paloušek D (2019) Effect of process parameters and high-temperature preheating on residual stress and relative density of Ti6Al4V processed by selective laser melting. Materials 12:930. https://doi.org/10.3390/ma12060930
82. Sato Y, Tsukamoto M, Shobu T, Yamashita Y, Yamagata S, Nishi T, Higashino R, Ohkubo T, Nakano H, Abe N (2018) Preheat effect on titanium plate fabricated by sputter-free selective laser melting in vacuum. Appl Phys A 124:288. https://doi.org/10.1007/s00339-018-1712-4
83. Ali H, Ma L, Ghadbeigi H, Mumtaz K (2017) In-situ residual stress reduction, martensitic decomposition and mechanical properties enhancement through high temperature powder bed preheating of Selective Laser Melted Ti6Al4V. Mater Sci Eng A 695:211–220. https://doi.org/10.1016/j.msea.2017.04.033
84. Ding CG, Cui X, Jiao JQ, Zhu P (2018) Effects of substrate preheating temperatures on the microstructure, properties, and residual stress of 12CrNi2 prepared by laser cladding deposition technique. Materials 11:2401. https://doi.org/10.3390/ma11122401
85. Kempen K, Vrancken B, Buls S, Thijs L, Humbeeck JV, Kruth JP (2014) Selective laser melting of crack-free high density M2 high speed steel parts by baseplate preheating. J Manuf Sci Eng 136:061026. https://doi.org/10.1115/1.4028513
86. Fallah V, Alimardani M, Corbin SF, Khajepour A (2010) Impact of localized surface preheating on the microstructure and crack formation in laser direct deposition of Stellite 1 on AISI 4340 steel. Appl Surf Sci 257:1716–1723. https://doi.org/10.1016/j.apsusc.2010.09.003
87. Zhang P, Ma L, Yuan JP, Cai ZH (2011) Analysis of stress and strain fields of laser cladding process on ring circular orbit. J Shanghai Jiaotong Univ 16:296–301. https://doi.org/10.1007/s12204-011-1147-y
88. Farahmand P, Kovacevic R (2014) An experimental-numerical investigation of heat distribution and stress field in single-and multi-track laser cladding by a high-power direct diode laser. Opt Laser Technol 63:154–168. https://doi.org/10.1016/j.optlastec.2014.04.016
89. Qi H, Mazumder J (2006) Numerical simulation of heat transfer and fluid flow in coaxial laser cladding process for direct metal deposition. J Appl Phys 100:024903. https://doi.org/10.1063/1.2209807
90. Zhao XR, Iyer A, Promoppatum P, Yao SC (2017) Numerical modeling of the thermal behavior and residual stress in the direct metal laser sintering process of titanium alloy products. Addit Manuf 14:126–136. https://doi.org/10.1016/j.addma.2016.10.005

91. Moat RJ, Pinkerton AJ, Li L, Withers PJ, Preuss M (2011) Residual stresses in laser direct metal deposited Waspaloy. Mater Sci Eng A 528:2288–2298. https://doi.org/10.1016/j.msea.2010.12.010
92. Pratt P, Felicelli SD, Wang L, Hubbard CR (2008) Residual stress measurement of laser-engineered net shaping AISI 410 thin plates using neutron diffraction. Metall Mater Trans A 39:3155–3163. https://doi.org/10.1007/s11661-008-9660-9
93. De Oliveira U, Ocelík V, De Hosson JTM (2006) Residual stress analysis in Co-based laser clad layers by laboratory X-rays and synchrotron diffraction techniques. Surf Coat Technol 201:533–542. https://doi.org/10.1016/j.surfcoat.2005.12.011
94. Andreas L, Robert P, Magnus HC, Craig B, Axel S, Almir H, Thomas B, Lars-Erik L (2016) Modeling and experimental measurement with synchrotron radiation of residual stresses in laser metal deposited Ti-6Al-4V. In: Proceedings of the 13th World Conference on Titanium, pp. 1279–1282. https://doi.org/10.1002/9781119296126.ch216
95. Biegler M, Graf B, Rethmeier M (2018) In-situ distortions in LMD additive manufacturing walls can be measured with digital image correlation and predicted using numerical simulations. Addit Manuf 20:101–110. https://doi.org/10.1016/j.addma.2017.12.007
96. Xu JJ, Lin X, Guo PF, Hu YL, Wen XL, Xue L, Liu JR, Huang WD (2017) The effect of preheating on microstructure and mechanical properties of laser solid forming IN-738LC alloy. Mater Sci Eng A 691:71–80. https://doi.org/10.1016/j.msea.2017.03.046
97. Rickenbacher L, Etter T, Hövel S, Wegener K (2013) High temperature material properties of IN738LC processed by selective laser melting (SLM) technology. Rapid Prototyp J 19:282–290. https://doi.org/10.1108/13552541311323281